



# A hybrid source mechanism of the 2017 M<sub>w</sub> 6.5 Jiuzhaigou earthquake revealed by the joint inversion of strong-motion, teleseismic and InSAR data

Ao Zheng<sup>a,b</sup>, Xiangwei Yu<sup>c</sup>, Wenbin Xu<sup>d,e,\*</sup>, Xiaofei Chen<sup>b</sup>, Wenbo Zhang<sup>c,\*\*</sup>

<sup>a</sup> School of Earth and Space Sciences, University of Science and Technology of China, Hefei, China

<sup>b</sup> Department of Earth and Space Sciences, Southern University of Science and Technology, Shenzhen, China

<sup>c</sup> College of Earth and Planetary Sciences, University of Chinese Academy of Sciences, Beijing, China

<sup>d</sup> School of Geosciences and Info-Physics, Central South University, Changsha, China

<sup>e</sup> Key Laboratory of Metallogenic Prediction of Nonferrous Metals and Geological Environment Monitoring (Central South University), Ministry of Education, Changsha, China

## ARTICLE INFO

### Keywords:

Jiuzhaigou earthquake  
Finite fault model  
Joint inversion  
InSAR  
Tectonic implications

## ABSTRACT

As occurred during the tourist season, the 2017  $M_w$  6.5 Jiuzhaigou (China) earthquake led to destructive damages. The seismogenic fault of this event was merely speculated to be the northern extension of the Huya fault, while no apparent surface ruptures were discovered in the field investigation. Previous studies and released moment tensor solutions indicated the Jiuzhaigou earthquake was dominated by left-lateral strike slip with partial normal-slip component. It seems unintelligible that the normal slip occurred in this event as the epicenter was located near the boundary of convergent blocks. Hence, a reasonable and elaborate source rupture model is necessary to investigate such a blind fault and the role it plays in the complex fault system of this region. Combining space-based geodetic, teleseismic or regional seismic observations can provide detailed information about earthquake ruptures. We first attempted to determine the fault geometry using the Bayesian approach with synthetic aperture radar interferograms (InSAR). And then the fault geometry was refined based on the relocated aftershock distribution, and a two-segment fault model was constructed. Based on the two-segment model, we resolved the source rupture process of the 2017 Jiuzhaigou earthquake through the joint inversion of strong-motion, teleseismic body-wave and InSAR data. The inversion results reveal a hybrid source mechanism, in which normal and thrust slips coexist besides the strike-slip component. We suggest that the eastward motion with the extrusion of the lower crustal flow in the northeastern margin of the Bayan Har block is responsible for such a faulting behavior. The co-seismic Coulomb stress changes show a significant stress loading in the western segment of the Tazang fault, increasing its seismic hazard. Due to the lack of aftershocks to the southeast of the seismogenic fault, the probably enhanced seismicity in the northern segment of the Huya fault is also worth further attention.

## 1. Introduction

A strong earthquake struck Jiuzhaigou County, Sichuan Province, China at 13:19:49 on 8 August 2017 (UTC), and caused 525 injuries and 25 casualties (Nie et al., 2018). The China Earthquake Networks Center (CENC) noted that the earthquake was a  $M_s$  7.0 event and its epicenter was located at 103.88°E and 33.20°N, with a focal depth of 20 km. The moment tensor solutions determined by the U.S. Geological Survey (USGS) and the Global Centroid Moment Tensor Project (GCMT) showed that the moment magnitude of the event was 6.5 and it was dominated by left-lateral strike slip. The Bayan Har block, a secondary

block of the Tibetan Plateau, has complex geological structures. The occurrence of the Jiuzhaigou earthquake on the northeastern edge of the Bayan Har block indicated that it is still tectonically active (Liu et al., 2006; Wang et al., 2007). Ren et al. (2017) suggested that the event resulted from the eastward extension of the eastern Kunlun fault at its eastern end. Xu et al. (2017) proposed the seismogenic fault of the earthquake was suspected to be the northern extension of the Huya fault due to similar kinematic properties, but there were no surface ruptures discovered in the field investigation. As the possible seismogenic fault might be a blind fault, it was not clearly identified in previous studies (Yi et al., 2017). Moreover, the motion features of the

\* Corresponding author.

\*\* Corresponding author at: College of Earth and Planetary Sciences, University of Chinese Academy of Sciences, Beijing, China.

E-mail addresses: [wenbin.xu@csu.edu.cn](mailto:wenbin.xu@csu.edu.cn) (W. Xu), [wenbo@ucas.ac.cn](mailto:wenbo@ucas.ac.cn) (W. Zhang).

seismogenic fault are still not well-known, and the role it plays in the complicated surrounding fault system of this region has only been inferred. Thus, a reasonable and elaborate source rupture model is urgently necessary.

Multiple studies have been carried out to understand the source rupture process of the Jiuzhaigou earthquake using different data sets and methods, among which Ji et al. (2017) and Sun et al. (2018) attributed the event to a source rupture of multiple faults. Ji et al. (2017) adopted a fault model containing two northeastward dipping segments, and determined the co-seismic slip distribution using InSAR data. Sun et al. (2018) indicated a complex source rupture consisted of three fault segments through the joint inversion of teleseismic body-wave and InSAR data, and proposed that the eastward extrusion of the Tibetan Plateau was responsible for the occurrence of the event. However, more studies chose to approximate the source geometry to a single planar fault model. Zhang et al. (2017) conducted a joint inversion of teleseismic and InSAR data, and discussed the optimal depth of the rupture starting point, which was finally determined as 11 km. Using teleseismic body-wave data, Xie et al. (2018) derived a source rupture model dominated by strike slip, in which there were two energy-releasing stages and the first one released most of the seismic moment. Nie et al. (2018) and Zhao et al. (2018) conducted the joint inversion of InSAR and Global Positioning System (GPS) displacement data. Zhao et al. (2018) suggested that the stress loading from the 2008 Wenchuan  $M_w$  7.9 earthquake had a triggering effect on the Jiuzhaigou event. Shan et al. (2017) inverted the Sentinel-1 interferograms using a single planar fault in which a slip asperity occurred. Most of previous source models show a strike-slip focal mechanism with a component of normal faulting, which is consistent with the released moment tensor solutions. However, the Jiuzhaigou earthquake was located near the boundary of convergent blocks. If the seismogenic fault were an extension of the Huya fault, a strike-slip and thrust fault, the focal mechanism should be controlled by the thrust slip besides the strike-slip component. In terms of regional tectonics, the conclusions resulted from previous studies seem inconsistent with the identified active faults. Therefore, an adequate and reasonable explanation is imperative for such a distinctive rupture pattern.

The extractable source information in a single type of data is limited, and data diversity can help to overcome the difficulties in source imaging that arise using only a single kind of data set (Melgar and Bock, 2015). After the Jiuzhaigou earthquake occurred, the strong-motion, teleseismic waveform records and InSAR data related to this event were all released and made available (Fig. 1). This provided us with a good opportunity and motivation to investigate a detailed spatiotemporal history of the source rupture using the joint seismo-geodetic inversion. In this study, when first assuming a planar fault as the source model of the Jiuzhaigou earthquake, we estimated the posterior probability distribution of fault geometry parameters using the Bayesian approach with InSAR data. Furthermore, delineated by the spatial distribution of relocated aftershocks, a refined two-segment fault model was determined. We adopted the two-segment source geometry and derived its rupture history from the joint inversion of several types of data sets. Afterwards, we calculated the co-seismic Coulomb stress changes in surrounding active faults, and evaluated their seismic hazard in the future. Finally, relating to regional tectonics, we attempted to explain the hybrid source mechanism of the 2017 Jiuzhaigou earthquake revealed by the joint inversion.

## 2. Finite fault model

The distribution of aftershocks relocated by Song et al. (2019) following the mainshock in 10 days shows that the aftershocks concentrate in a north-west oriented band (Fig. 2a), which is close to the strike direction of the Huya fault located to the south. However, there were no obvious surface breaks captured in the earthquake (Xu et al., 2017), so we could not yet simply associate the unmapped seismogenic

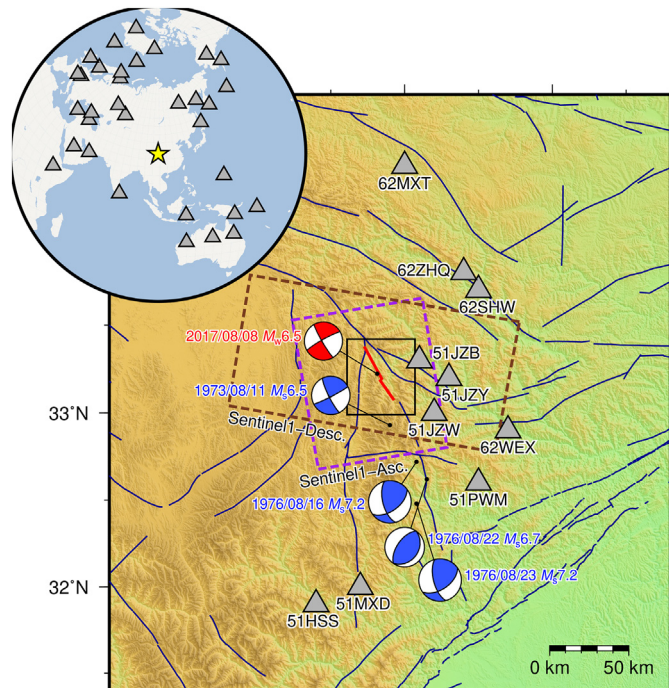


**Fig. 1.** Study area map of the 2017  $M_w$  6.5 Jiuzhaigou earthquake. The beach ball in red shows the focal mechanism of the Jiuzhaigou earthquake derived from the joint inversion, and the red lines are the projected top edge traces of the two-segment fault model. Gray triangles indicate the strong-motion and teleseismic stations (in the hemispherical inset) used in this study. The colored dashed frames represent the coverage of Sentinel-1 interferograms. The black frame indicates the area illustrated in Fig. 2a. Dark blue lines depict the active faults in this region (Deng et al., 2003). The focal mechanisms of the 1973 Songpan-Huanglong earthquake and the 1976 Songpan sequence are also shown in blue. (For interpretation of the references to colour in this figure legend, the reader is referred to the web version of this article.)

fault with a northern extension of the Huya fault. Though the surface deformation acquired by InSAR images has dense observations that are sensitive to the fault geometry, the fault geometry is not able to be directly recognize due to the severe loss of coherence in the near-field of the source region, where the lush vegetation and rugged terrains strongly influenced the imaging capability of the C-band Sentinel-1 satellite. To determine the geometry of such a blind seismogenic fault, based on the hypothesis of a single planar fault, we adopted the Bayesian approach to estimate the posterior probability distribution of model parameters using InSAR data.

### 2.1. InSAR observation

Two Sentinel-1 interferograms acquired both in ascending and descending orbits were used to retrieve the co-seismic ground deformation that covers the epicenter area (Table 1). Following the standard two-pass InSAR data processing method (Xu et al., 2016), we processed the interferograms with GAMMA software and utilized the 30 m Shuttle Radar Topography Mission digital elevation model (SRTM DEM) to simulate and eliminate the topographic signals (Farr et al., 2007). To increase the signal-to-noise ratio (SNR), the interferograms were multi-looked to an approximately 30 m pixel spacing. The interferograms were then filtered with an improved Goldstein filter (Li et al., 2008) and unwrapped using the minimum cost flow method (Chen and Zebker, 2001). Afterwards, the unwrapped interferograms were geocoded into the World Geodetic System 84 (WGS84) coordinate system. Finally, we carefully checked the results of phase unwrapping, and masked out areas with low coherence in which some remaining unwrapping errors could not be corrected. Considering the large amount

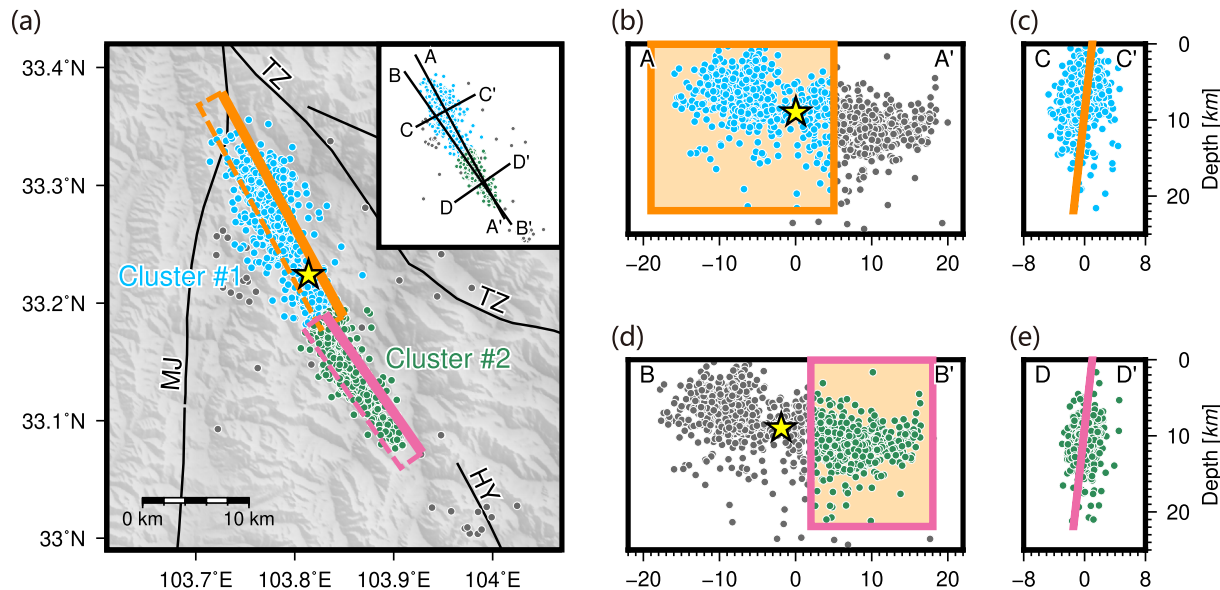


**Fig. 2.** (a) Distribution of the aftershock sequence ( $M \geq 1$ ) following the mainshock in 10 days. The blue and green circles indicate the aftershocks of Cluster #1 and Cluster #2, respectively. The gray circles are the aftershocks that cannot be projected into two segments. The orange and pink frames are separately the projections of the northern and southern segments. The yellow star depicts the epicenter of the mainshock. Fault abbreviations are TZ: Tazang fault, MJ: Minjiang fault, HY: Huya fault. (b) Cross-section A-A' that is parallel to the strike of the northern segment. (c) Cross-section C-C' that is perpendicular to the strike of the northern segment. The colored plane with an orange frame in (b) and the orange line in (c) both represent the projection of the northern segment. (d) Cross-section B-B' that is parallel to the strike of the southern segment. (e) Cross-section D-D' that is perpendicular to the strike of the southern segment. The colored plane with a pink frame in (d) and the pink line in (e) both represent the projection of the southern segment. The yellow star in (b) and (d) indicates the hypocenter of the mainshock. (For interpretation of the references to colour in this figure legend, the reader is referred to the web version of this article.)

of data points in unwrapped interferograms, we subsampled them using the quadtree method without losing significant information (Jónsson et al., 2002).

## 2.2. Bayesian estimation for fault geometry

Bayesian methods use probability models in inverse problems to quantify our state of knowledge by explicitly treating the uncertainties related to the observation process and the uncertainties due to missing information or model errors, and from this we can ascribe a posterior plausibility to each model in a set of proposed models (Jaynes, 2003; Beck, 2010). This posterior probability distribution describing the plausibility of each member of the ensemble of models is the “solution” to our inverse problem (Minson et al., 2013). Considering a model parameter vector,  $\mathbf{m}$  in the  $M$ -dimensional model space relating to the data vector  $\mathbf{d}$  in the  $N$ -dimensional data space:  $\mathbf{d} = G(\mathbf{m}) + \epsilon$ , where  $G(\mathbf{m})$  is the forward modeling operator with  $\epsilon$  error. Depending on the Bayesian approach, it allows us to use the prior information to obtain an estimation of the posterior probability distribution of model parameters to a generic inverse problem (Tarantola, 2005; Bagnardi and Hooper, 2018; Dutta et al., 2018):

$$p(\mathbf{m} | \mathbf{d}) = \frac{p(\mathbf{d} | \mathbf{m})p(\mathbf{m})}{p(\mathbf{d})}, \quad (1)$$

where  $p(\mathbf{d} | \mathbf{m})$  is the likelihood function of  $\mathbf{m}$  given  $\mathbf{d}$  based on residuals between the data and the predicted observation with  $\mathbf{m}$ ,  $p(\mathbf{m})$  expresses the prior information of model parameters, and the denominator is a normalizing constant independent of  $\mathbf{m}$ . When we consider the

observed data to have Gaussian uncertainties with zero mean and covariance matrix  $\Sigma_d$ , the likelihood function is described as following:

$$p(\mathbf{d} | \mathbf{m}) = \frac{1}{(2\pi)^{N/2} |\Sigma_d|^{1/2}} \exp \left[ -\frac{1}{2} (\mathbf{d} - \mathbf{G}(\mathbf{m}))^T \Sigma_d^{-1} (\mathbf{d} - \mathbf{G}(\mathbf{m})) \right]. \quad (2)$$

While the prior information of model parameters is often unavailable, in which case a so-called uninformative Jeffreys prior is used (Jeffreys, 1983; Ulrych et al., 2001; Bagnardi and Hooper, 2018). In the framework of the Bayesian Earthquake Analysis Tool (BEAT), developed by Vasyura-Bathke et al. (2020) based on the Python seismology toolbox Pyrocko (Heimann et al., 2017), the prior distribution of each model parameter is set as independent and uniform with a finite range of possible values, and the upper and lower bounds can be added outside which  $p(\mathbf{m}) = 0$ . Afterwards, the BEAT package implements the Sequential Monte Carlo (SMC) sampling algorithm (Minson et al., 2013) to evaluate the high-dimensional posterior probability distribution. The SMC sampling algorithm is based on the Transitional Markov Chain Monte Carlo (TMCMC) algorithm of Ching and Chen (2007) that combines transitioning and resampling with the Markov Chain Monte Carlo (MCMC) simulation of the Metropolis algorithm (Metropolis et al., 1953). It outperforms the unparallelizable Metropolis algorithm as sampling a probability distribution function (PDF) with multiple Markov chains, which makes the sampling more efficient (Minson et al., 2013).

Given the line-of-sight (LOS) displacement data retrieved from two Sentinel-1 interferograms, we used BEAT to estimate the posterior PDF of the fault geometry parameters. Fig. 3 shows the resulting histograms

**Table 1**

Sentinel-1 interferograms used in this study.

Sensor	Master (yy/mm/dd)	Slave (yy/mm/dd)	Before (day)	After (day)	Perpendicular baseline (m)	Orbit	Incidence angle (deg.)
Sentinel-1	2017/07/30	2017/08/11	9	3	36	Ascending	43.8
Sentinel-1	2017/08/06	2017/08/18	2	10	-67	Descending	39.2

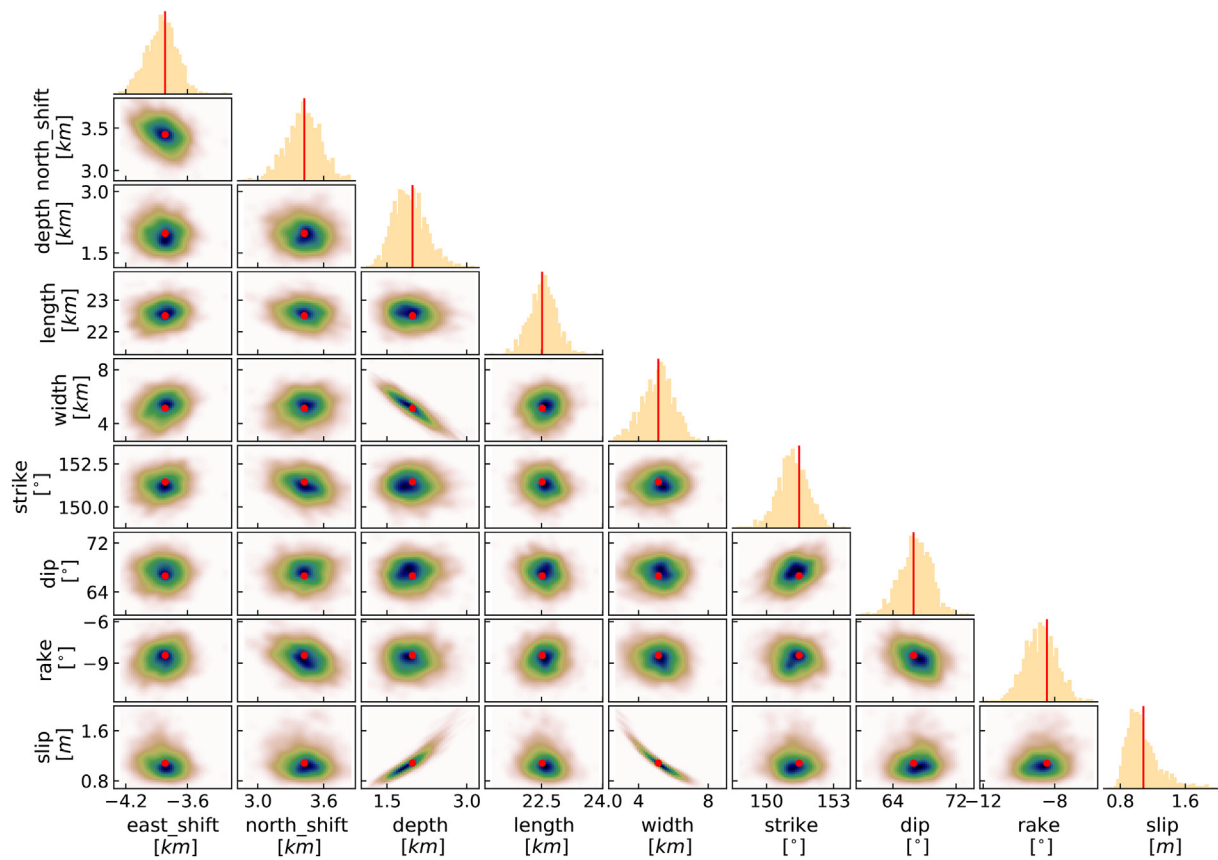


**Fig. 3.** 1-D and 2-D posterior PDF plots of the fault geometry parameters derived from the Bayesian estimation using InSAR data. Red lines in the 1-D PDF plots and red points in the 2-D PDF plots show the best-fit values of parameters. Cold colors in the 2-D PDF plots show high probability region, and warm colors show low probability region. (For interpretation of the references to colour in this figure legend, the reader is referred to the web version of this article.)

of 1-D marginal PDF for each parameter and the plots of 2-D joint PDF for each parameter pair. The optimal values of the model parameters correlate well with the peaks of the Bayesian estimation (the predicted InSAR data and residuals are shown in Fig. S1). According to the 95% confidence interval given by the inversion, the InSAR data can be well explained by the slip on a 21.9–23.1 km-long, 3.3–6.8 km-wide fault, striking  $150.1^\circ \sim 152.6^\circ$  and steeply dipping at  $62.8^\circ \sim 70.2^\circ$ . The 0.8–1.5 m slip with a  $-10.4^\circ \sim -7.0^\circ$  rake is consistent with the focal mechanism of left-lateral strike-slip fault with a minor normal-slip component. Assuming a shear modulus of  $3.0 \times 10^4$  MPa, the moment magnitude corresponding to the best-fit geometry model is equal to 6.4, slightly less than the magnitude of 6.5 reported by GCMT and USGS. The 2-D marginal PDF plots clearly show the trade-offs between fault width, depth and slip. Conversely, the shift distance of the epicenter, the length, strike, dip of the fault plane, and the rake direction can be well constrained. The seismogenic widths of strike-slip faults play an important role in rupture propagation and are usually less than 20–30 km. There appears to be a boundary near the width of 10 km where the aspect ratio (the ratio between the length and width of rupture extent) increases drastically. If the seismogenic width is less than the critical width, then the rupture will become self-arresting and the aspect ratio is generally less than 8 (Weng and Yang, 2017). Under the hypothesis of uniform slip in the Bayesian approach, the aspect ratio estimated from the 95% confidence interval of length and width is 3.2–7.0, which implies the width may control the rupture length. The upper limit of the 95% confidence interval of width is less than the critical value of 10 km, however, the expanding range of aftershocks in depth has exceeded 20 km (Fig. 2). It is possible that a subcritical seismogenic width is not adequate to accommodate the whole rupture extent. In order to investigate the rupture extent and the inhomogeneity

of fault slip, an inversion of slip distribution is necessary, and the size of the fault plane, especially the width should be large enough to naturally vanish the parameter trade-offs generated from the Bayesian estimation.

### 2.3. Slip distribution derived from InSAR data

To determine details of the slip distribution, fixing the strike and dip of the fault plane according to the optimal model parameters estimated from the Bayesian approach, we enlarged the fault plane as  $40 \text{ km} \times 22 \text{ km}$ , and then discretized it into 220 subfaults, among which each one possessing a size of  $2 \text{ km} \times 2 \text{ km}$ . We used the epicenter located by USGS,  $103.855^\circ\text{E}$  and  $33.193^\circ\text{N}$ , as the initial value in the Bayesian inversion. Based on the shift distances of the epicenter in both east-west and north-south directions revealed by the Bayesian inversion, the updated hypocenter is located at  $103.814^\circ\text{E}$  and  $33.224^\circ\text{N}$  with a depth of 9 km. The optimal fault dip indicated by the Bayesian estimation is  $66.6^\circ$ , while the previous studies and released focal mechanisms all indicated a steeper fault plane ( $> 70^\circ$ ). The uniform slip distribution hypothesis in the Bayesian estimation and the loss of coherence of InSAR data in near-field might not efficiently constrain the fault dip. To obtain a more plausible finite fault model, fixing other parameters estimated from the Bayesian inversion, we conducted static inversions with InSAR displacement data to determine the fault dip by grid search technique. Starting from the dip of  $66.6^\circ$  to nearly  $90^\circ$  with an increment of  $1^\circ$ , the trade-off curve between the tested values and the normalized misfit is shown in Fig. 4a. The trade-off curve illustrates that the dip of  $83.6^\circ$  generates the best fit of InSAR data, we selected it as the fault dip. In addition, the strike was set as  $151.4^\circ$ , and the rake direction of subfaults was limited within  $0^\circ \pm 45^\circ$  mainly allowing

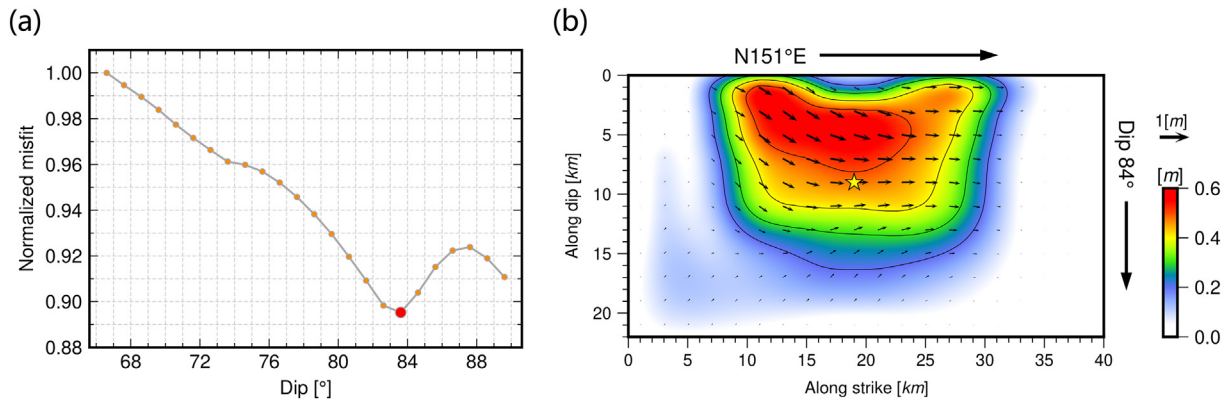


**Fig. 4.** (a) Trade-off curve between the fault dip and the normalized misfit in static inversion trials using InSAR data. The red solid circle shows the preferred dip. (b) Co-seismic slip distribution determined by the inversion of InSAR data with the preferred fault dip. The slip contour interval is 0.1 m and the yellow star indicates the hypocenter. (For interpretation of the references to colour in this figure legend, the reader is referred to the web version of this article.)

sinistral fault slips. The corresponding co-seismic slip distribution is shown in Fig. 4b, in which the focal mechanism is dominated by strike slips with a mixture of normal slips and few reverse slips. Large slips mainly occur in the northwest at the shallow depth, but are weakened near the top edge of the fault plane. The released seismic moment is  $5.3 \times 10^{18}$  N·m ( $M_w$  6.4), and the peak slip is close to 0.6 m, which is slightly small for an event of magnitude  $\sim$ 6.5. We think the absence of near-field displacement that greatly affected the amount of slips, may cause the underestimation of the peak slip and the releasing moment.

#### 2.4. Two-segment fault delineated by aftershocks

From a rough map-view perspective, the relocated aftershocks seem to linearly distribute along a north-west strike. The InSAR data were well resolved by the static inversion using a single planar fault model. However, as shown in Fig. 2a, a slight deflection from north to south in the extending orientation is not difficult to be found in the horizontal distribution of aftershocks. It is particularly obvious that the two ends of the band zone where most aftershocks concentrate have different strike directions. The occurrence of the slight deflection is located close to 33.2°N, so we took this position with its vicinity as a boundary. And the aftershocks were divided into two clusters following the boundary. The distributed orientation of Cluster #1 is consistent with the strike of the single planar fault, which was used in the aforementioned static inversion of InSAR data. While the aftershocks of Cluster #2 appear to follow a strike direction of 145°. This implies a more complex seismogenic structure rather than a single planar fault. To obtain a more reasonable source geometry, we attempted to construct a two-segment fault model to match the spatial distribution of two aftershock clusters. The strike of the northern segment was set as 151.4° with a length of 24 km, and the southern segment oriented following the strike of 145° with a length of 16 km. Both segments had a width of 22 km and a common dip of 83.6°. The hypocenter (rupture starting point) was placed in the northern segment. In Fig. 2, we set up four cross-sections, among which A-A' and B-B' are parallel to the strike directions of the northern and southern segments respectively, and cross-sections C-C' and D-D' are separately perpendicular to A-A' and B-B'. The aftershocks of two clusters were separately projected into cross-sections A-A' and B-B'. In cross-section A-A' (Fig. 2b), most aftershocks of Cluster #1 are localized at the depth less than 15 km. While the aftershocks of Cluster #2 mainly concentrate at the depth of 5–16 km in cross-section B-B' (Fig. 2d). Moreover, the projections of two fault segments in cross-sections C-C' and D-D' both show a good fit between the fault dip and the aftershock distribution (Fig. 2c and Fig. 2e). Hence, this two-segment fault model delineated by the aftershock distribution can help us to reconstruct the elaborate history of the source spatiotemporal rupture in the Jiuzhaigou earthquake.

### 3. Joint inversion

Combining multiple types of data for studying the source rupture process has become a developing trend in source kinematic inversions. We can extract the spatiotemporal evolution process of earthquake source rupture from seismic waveform records. Compared with the teleseismic body-wave, the regional strong-motion data contain more high-frequency information related to rupture details due to weak attenuation (Hartzell and Heaton, 1983; Sekiguchi et al., 2000; Sekiguchi and Iwata, 2002; Zheng et al., 2018). The teleseismic body-wave data implying the general characteristics in the source rupture area, can be effectively complementary to the resolution capability of strong-motion data. InSAR data that has been widely used to measure the co-seismic ground deformation since the 1992 Landers earthquake (Massonnet et al., 1993; Jónsson et al., 2002; Xu, 2017), are helpful in determining co- or post-seismic slip distribution (Xu et al., 2018; Liu and Xu, 2019). Hence, the combination of multiple data sets for a joint inversion will generate a more robust picture of the source rupture (Delouis et al., 2002). Based on the two-segment fault model delineated by the aftershock distribution, combining the InSAR data used in the Bayesian estimation with the strong-motion and teleseismic waveform data, we conducted a joint inversion to derive the source rupture process of the Jiuzhaigou earthquake.

#### 3.1. Strong-motion and teleseismic waveforms

Owing to complicated geomorphologic conditions, strong-motion stations are not densely distributed in the vicinity of the epicenter. We used the three-component strong-motion acceleration waveform records at 10 stations of the China Strong Motion Network operated by the Institute of Engineering Mechanics, China Earthquake Administration (CEA). Their epicentral distance ranges from 30 km to 150 km. The initial strong-motion data had been preprocessed, integrated into velocity waveforms, filtered between 0.05 and 0.6 Hz, and resampled at 5 Hz. The strong-motion stations are indicated by the gray triangles with station names in Fig. 1.

The teleseismic body-wave data were provided by the Data Management Center of the Incorporated Research Institutions for Seismology (IRIS DMC). To improve the azimuthal coverage for the source area, we selected 33 vertical components of  $P$ -wave with epicentral distance ranging between 30° and 90°. The instrument response was removed from initial records to obtain velocity waveforms with a better spatiotemporal resolution (Wald et al., 1996). Similar to the strong-motion data, the teleseismic waveforms were integrated into displacement data, filtered between 0.02 and 0.1 Hz and resampled at 5 Hz. The teleseismic stations are indicated by the gray triangles in the hemispherical inset of Fig. 1.

### 3.2. Inversion methodology

We used the multi-time-window linear inversion strategy (Olson and Apsel, 1982; Hartzell and Heaton, 1983; Sekiguchi et al., 2000; Sekiguchi and Iwata, 2002) to estimate the kinematic source rupture process of the 2017 Jiuzhaigou earthquake. In this method, the rupture history is discretized in both space and time domains. The linear relationship between the source model and the observed data (displacement, velocity or acceleration records) is constructed based on the representation theorem (Aki and Richards, 2002). For discretization in space domain, the finite fault plane is divided into small subfaults, and each subfault is regarded as an independent point source when satisfying the far-field hypothesis. For discretization in time domain, the moment releasing history of a subfault is represented by several time-window functions. Based on the representation theorem, the observational equation is described as following:

$$\dot{U}(t) = \sum_{if=1}^{nf} \sum_{islip=1}^{nslip} \sum_{itw=1}^{ntw} m_{if, islip, itw} T(t - \Delta t_{trig}) * \dot{G}_{if, islip}(t), \quad (3)$$

with  $1 \leq if \leq nf$ ,  $1 \leq itw \leq ntw$ ,  $1 \leq islip \leq nslip$  ( $nslip = 2$ ).

Here, the subscripts  $if$ ,  $itw$ ,  $islip$  are indices for the subfault, time-window function and slip direction, respectively. More details were described in Zheng et al. (2018). According to the observational equation, a projection from the model space to the data space can be constructed using the Green's function matrix to obtain a modified matrix form of the observational equation as below,

$$\begin{bmatrix} \mathbf{G}_S \\ \mathbf{G}_T \\ \mathbf{G}_I \\ \lambda(\mathbf{S}_t) \end{bmatrix} \mathbf{m} \cong \begin{bmatrix} \mathbf{d}_S \\ \mathbf{d}_T \\ \mathbf{d}_I \\ (0) \\ (0) \end{bmatrix}. \quad (4)$$

In this equation,  $\mathbf{G}_S$  and  $\mathbf{G}_T$  are separately the matrices of Green's functions of strong-motion and teleseismic body-wave convolved with the time-window function.  $\mathbf{G}_I$  is the Green's function matrix of InSAR data, namely, the projection of Green's functions of the ground deformation displacement into the satellite LOS direction. As a static observation of the ground deformation,  $\mathbf{G}_I$  should be extended into multiple time-windows to satisfy the model parameter vector  $\mathbf{m}$ . We used the frequency wavenumber integration code provided by Zhu and Rivera (2002) to calculate Green's functions for strong-motion and InSAR data sets. For the station side of strong-motion records and the source region, the velocity model (Table S1) was assumed as a horizontally layered structure (Shen et al., 2016) modified by empirical relations of Brocher (2005). Based on the crustal structure of CRUST1.0 model (Laske et al., 2013) with the mantle and core parts of the AK135 reference earth model (Kennett et al., 1995), the Green's function of teleseismic body-wave were generated by Multitel3 developed by Qian et al. (2017) with considering both direct and core-reflected waves.  $\mathbf{d}_S$

and  $\mathbf{d}_T$  are the strong-motion and teleseismic body-wave data vectors, respectively.  $\mathbf{d}_I$  is the InSAR data vector. Following Chen et al. (2018), we normalized all data sets by their own Frobenius norms. After several trials, our preferred weighting scheme for the InSAR, strong-motion and teleseismic data sets is 1.0, 0.4, 0.25, respectively.  $\mathbf{S}_t$  and  $\mathbf{S}_s$  are the temporal and spatial smoothing constraint matrices, respectively, which are imposed on the source model parameter to stabilize the inversion problem and obtain a physically reasonable result.  $\lambda$  is a scalar coefficient that controls the smoothing strength. The nonnegative least-squares algorithm developed by Lawson and Hanson (1974) was used to solve the observational equation.

In addition, we developed a revised form of the differential smoothing constraint based on that proposed by Yagi et al. (2004). The conventional differential form of the smoothing constraint is separated in time and space domains. The smoothing with respect to time domain is:

$$\left\{ \begin{array}{l} m_{ix, iw, islip, itw-1} - 2m_{ix, iw, islip, itw} + m_{ix, iw, islip, itw+1} = 0 \\ m_{ix, iw, islip, 0} = m_{ix, iw, islip, itw+1} = 0 \end{array} \right.. \quad (5)$$

The smoothing constraint with respect to space domain is introduced by a Laplacian finite-difference operator:

$$\left\{ \begin{array}{l} \sum_{itw=1}^{ntw} m_{ix-1, iw, islip, itw} + m_{ix+1, iw, islip, itw} \\ + m_{ix, iw-1, islip, itw} \\ + m_{ix, iw+1, islip, itw} - 4m_{ix, iw, islip, itw} = 0 \\ m_{0, iw, islip, itw} = m_{ix+1, iw, islip, itw} = m_{ix, 0, islip, itw} \\ = m_{ix, iw+1, islip, itw} = 0 \end{array} \right., \quad (6)$$

where the subscripts  $ix$  and  $iw$  are indices of the  $ix$ -th subfault in the strike direction and the  $iw$ -th subfault in the downdip direction, respectively. The conventional smoothing constraint requires two hyper-parameters to separately control the temporal and spatial smoothing strengths. It is difficult to look for optimal values of two hyper-parameters in an extraordinarily wide range by grid search, also not suitable for rapid inversions. Thus, we attempted to use a single hyper-parameter to control two smoothing constraints simultaneously and facilitate the emergence of the optimal. This requires that the revised smoothing constraint can adaptively adjust its smoothing strength according to the geometric size of the earthquake source model. The spatial smoothing constraint (Fig. 5a) is imposed on one subfault (coefficient of the time-window is  $m_0$ ) and  $n$  adjacent subfaults (coefficients of the time-windows are  $m_1, m_2, \dots, m_n$ ),

$$\omega_0 \cdot \left( \sum_{i=1}^n m_i \omega_i - 4m_0 \right) = 0, \quad (7)$$

in which,

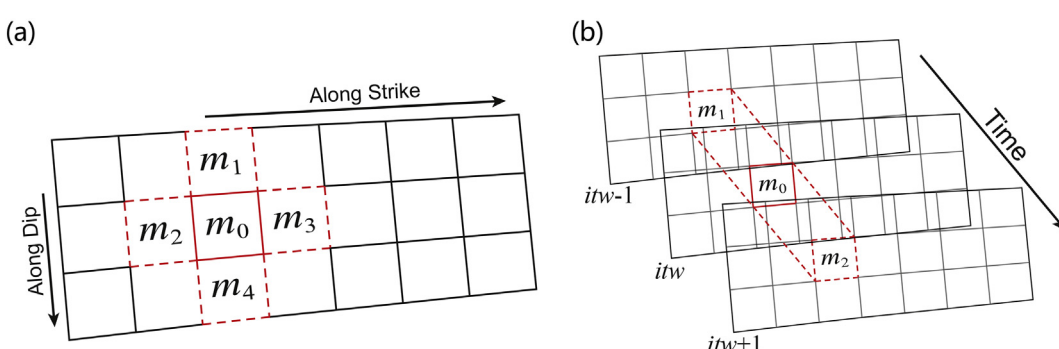


**Fig. 5.** Schematic description of the smoothing constraint, referring to Funning et al. (2014). (a) Spatial smoothing. (b) Temporal smoothing. (For interpretation of the references to colour in this figure legend, the reader is referred to the web version of this article.)

$$\begin{aligned}\omega_0 &= \left( \prod_{i=1}^n t_m / \Delta t_i \right)^{1/n}, \\ \omega_i &= \frac{1/\Delta t_i}{\sum_{i=1}^n 1/\Delta t_i} \cdot n, \\ \Delta t_i &= |t_i - t_0|, \quad (i = 1, \dots, n; n = 2 \sim 4)\end{aligned}\quad (8)$$

Here,  $t_m$  is the maximum triggering time of the first time-window, proportional to the fault size.  $t_0$  and  $t_i$  are the triggering times of the constrained subfault and adjacent subfaults, respectively.  $\omega_0$  is the smoothing weight for the individual constraint of a subfault related to the geometric size of the whole rupture extent.  $\omega_i$  expresses the relative weight of smoothing on the subfault constrained by adjacent subfaults. The temporal smoothing constraint (Fig. 5b) is imposed on one time-window (coefficient of the time-window is  $m_0$ ) and two neighboring time-windows (coefficients of the time-windows are  $m_1$  and  $m_2$ ),

$$\omega_0 \cdot \left( \sum_{i=1}^n m_i \cdot \omega_i - 2m_0 \right) = 0, \quad (9)$$

in which,

$$\begin{aligned}\omega_0 &= \left( \prod_{i=1}^n t_m / \Delta t_i \right)^{1/n}, \\ \omega_i &= \frac{1/\Delta t_i}{\sum_{i=1}^n 1/\Delta t_i} \cdot n, \\ \Delta t_i &= dtw, \quad (i = 1, \dots, n; n = 2)\end{aligned}\quad (10)$$

Since the time-window interval  $dtw$  is always constant between each pair of neighboring time-windows, the temporal smoothing constraint can be further simplified into

$$\begin{aligned}\omega_i &= 1, \\ \omega_0 \cdot \left( \sum_{i=1}^n m_i - 2m_0 \right) &= 0.\end{aligned}\quad (11)$$

A number of inversion trials were conducted to determine the optimal value of the single hyper-parameter, and the preferred smoothing factor was selected as 0.016 (Fig. S2). Considering the trade-off between the rupture propagating velocity (the triggering speed of the first time-window) and the rise time, we also tested the prescribed rupture velocity from 2.2 km/s to 3.2 km/s (corresponding to 60–90% of the local S-wave speed) with an interval of 0.2 km/s, and the rise time of time-window from 0.8 s to 2.4 s with an interval of 0.2 s (Fig. S2). Finally, the prescribed rupture velocity was selected as 3.2 km/s, allowing a maximum rise time of 8.0 s within 7 triangle time-windows.

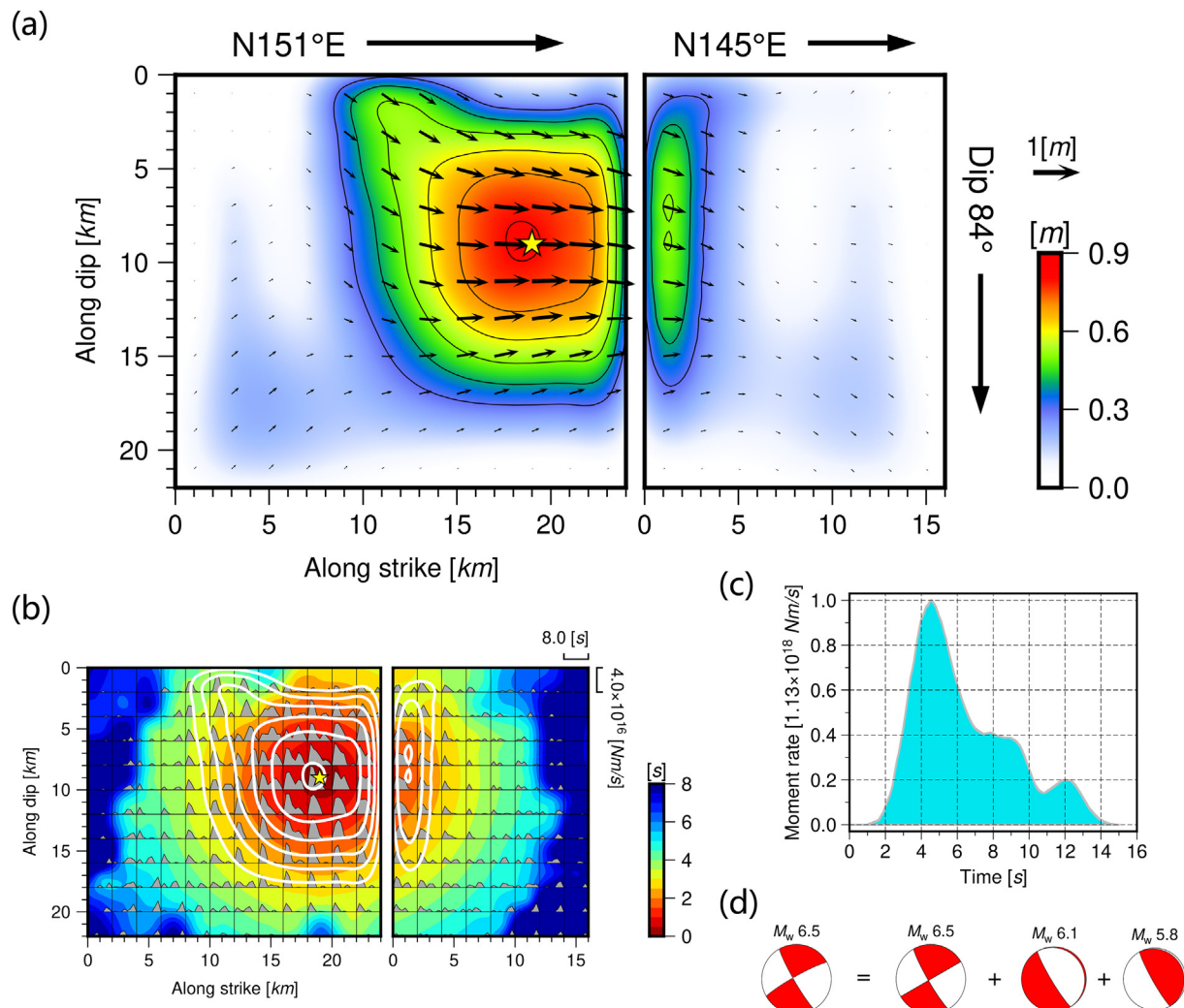
#### 4. Results

Fig. 6a shows the final slip distribution derived from the joint inversion. The source rupture model releases a scalar seismic moment of  $7.9 \times 10^{18}$  N·m ( $M_w$  6.5). A large asperity occurs in the northern segment, extending for about 15 km along the downdip direction from the top edge. Significant slips dominated by left-lateral strike-slip component concentrate in this large patch and center at the rupture starting point. The peak slip of 0.8 m also occurs at the rupture starting point. Slips in the southern segment concentrate on its northern side, and up to about 0.5 m. The uppermost slips of two segments are not comparable with those at depth, implying that such a shallow earthquake cannot generate surface breaks. The comparison of relocated aftershocks and the final slip distribution is depicted in Fig. S3. In the northern segment, most aftershocks occur in the large slip patch but surround the rupture starting point. This is consistent with that regions

of sharp changes from high to low slip in the interior of the rupture area often have aftershocks (Das and Henry, 2003). Meanwhile, plenty of aftershocks are located in the less slipped area of the southern segment. The increased stress caused by the mainshock possibly contributes to the complementary aftershock distribution. Taken as a circular fault, the large slip patch has a radius ( $R$ ) of 8 km and an average slip ( $\bar{D}$ ) of 0.6 m. With a shear modulus ( $\mu$ ) of  $3.0 \times 10^4$  MPa, the average stress drop ( $\Delta\sigma$ ), estimated using the expression  $\Delta\sigma = \frac{7\pi}{16} \mu \frac{\Delta\bar{D}}{R}$  (Kanamori and Anderson, 1975), is about 3.1 MPa. This is consistent with previous observations of stress drop that were usually less than 5.0 MPa in western China (Cheng et al., 2020).

In addition, the slip distribution shows a rather strange faulting pattern, in which the normal and thrust slips coexist in a single event, besides the desired strike-slip component. The normal slips are obvious at the shallow depth in both segments, but decrease along the downdip direction. While in the deep part of two segments, the thrust slips dominate and almost only occur in this area. Furthermore, we synthesized the focal mechanism from the cumulative moment tensor of subfaults through Pyrocko (a seismic analysis toolbox based on Python, developed by Heimann et al. (2017)). An ordinary focal mechanism was obtained, whose equivalent rake is  $-7^\circ$  (Fig. 6d). Apart from a normal-slip component ( $M_w$  6.1), the decomposition of the cumulative moment tensor also shows a thrust component ( $M_w$  5.8) estimated from the joint inversion. Apparently, the slip distribution reveals more about the inhomogeneous source rupture compared with the point-source moment tensor, and indicates that the seismogenic fault plays a special role in regional tectonics. The Tazang fault, the eastern terminus of the eastern Kunlun fault to the north of the seismogenic fault, is dominated by purely strike slip. But the faulting mechanism of the northern segment of the Huya fault or the Minjiang fault is controlled by left-lateral strike slip and thrust slip. As the strike changes from east-west of the Tazang fault to nearly north-south of the Huya fault, the motion of the Bayan Har block accommodated by its northeastern margin is converted from purely strike slip into a mixture of sinistral strike slip and thrust slip. However, the thrust component of the Jiuzhaigou event estimated from the joint inversion is not comparable to that of strike slip, and almost cancelled out by the larger normal-slip component in the cumulative moment tensor. This demonstrates that the motion property of the seismogenic fault is between the Tazang fault and the northern segment of the Huya fault. The seismogenic fault is a transition zone between the Tazang fault and the Huya fault, and connects them together to form a part of the horsetail-shaped structure of the eastern Kunlun fault system. Details are discussed in the following section.

Fig. 6b shows the moment releasing rate function of each subfault. Subfaults in the asperity area start to rupture instantaneously as long as the first time-window is triggered by a prescribed rupture velocity. Most of subfaults at depth possess a source time function that seems like a unimodal pulse, and larger slip often corresponds to a longer duration. While those in the shallow part of the fault plane have a more complex source time function, and are releasing seismic moment throughout the maximum allowed duration. At the first 2 s of the source process, the rupture expands outwards following a circular pattern, after which the rupture propagating front turns into an uneven shape. Since the first time-windows of a few subfaults are not triggered, the rupture front turns into a heterogeneously bilateral extension. The snapshots of the source rupture process are presented in Fig. 7. The source model indeed shows a bilateral rupture pattern, and the total duration is nearly 15 s. The source rupture starts in the northern segment, and then the rupture front propagates into the southern segment after about 2 s. The rupture of the asperity in the northern segment starts from the onset of the whole source process and lasts approximately 10 s. This is consistent with the cumulative moment releasing rate function illustrated in Fig. 6c, in which the energy releasing process consists of two stages. The first stage, which starts from the rupture initiation, results in a large slip patch and lasts approximately 10 s,



**Fig. 6.** (a) Final slip distribution derived from the joint inversion. The slip contour interval is 0.1 m and the yellow star indicates the rupture starting point. (b) Seismic moment releasing rate functions of subfaults in the two-segment fault model. The background is the rupture front evolution with respect to time. The slip contour is also plotted in white lines. (c) Cumulative seismic moment releasing rate function of the two-segment fault model. (d) Cumulative moment tensor of the final slip distribution that can be decomposed into a  $M_w$  6.5 strike-slip component, a  $M_w$  6.1 normal-slip component and a  $M_w$  5.8 thrust-slip component. (For interpretation of the references to colour in this figure legend, the reader is referred to the web version of this article.)

reaching its maximum moment rate at about 4.5 s and releasing the majority of earthquake energy. After this peak, the moment rate starts to decrease but becomes flat in 7–9 s, and then continues to decrease. The second stage may be attributed to minor slips in remaining rupture areas of the fault plane, which corresponds to the last 5 s of the total rupture.

Fig. 8 compares the observed records and synthetic waveforms of strong-motion and teleseismic  $P$ -wave. Data of all strong-motion stations and most of teleseismic stations are well resolved, but the initial motions at a few teleseismic stations with azimuth  $272^\circ \sim 339^\circ$  cannot be modeled with good fit. In the study of Sun et al. (2018), a thrust subevent initiated at the hypocenter were resolved by a multipoint source inversion to fit the initial waveforms. Nevertheless, the absence of the structure in our source model related to such a thrust subevent, does not generate significant influences on modeling the near-field data of strong-motion and InSAR. Moreover, the thrust structure proposed in Sun et al. (2018) is too small to directly identify from the aftershock distribution. More investigations will be needed to verify the existence of the small thrust structure and the source complexity implied by the teleseismic data. The moment tensor solutions of similar thrust aftershocks should provide strong support. It is necessary to extract the moment tensor solutions of some typical aftershocks near the

hypocenter because the thrust subevent was located there. Apart from the waveform data, the comparison between two observed InSAR images and the predicted data are presented in Fig. 9 and Fig. S4, both for the unwrapped displacement and wrapped interferograms of ground deformation. The fit in the near-field area of the descending image is not comparable to that in the ascending image, because the corresponding areas were masked during preprocessing due to the severe loss of coherence.

## 5. Discussion

### 5.1. Co-seismic Coulomb stress changes

The seismic stress triggering theory indicates that regional stress accumulated by tectonic motion is released when earthquakes occur. The accumulated stress does not vanish immediately, but is redistributed through the process of stress transfer, which may trigger successive earthquakes. The positive change of Coulomb failure stress (CFS) increases stress loading in certain regions and enhances the possible seismicity and vice versa (King et al., 1994; Stein et al., 1994). In order to understand the probable change of regional seismicity induced by the 2017 Jiuzhaigou earthquake, we calculated the co-seismic

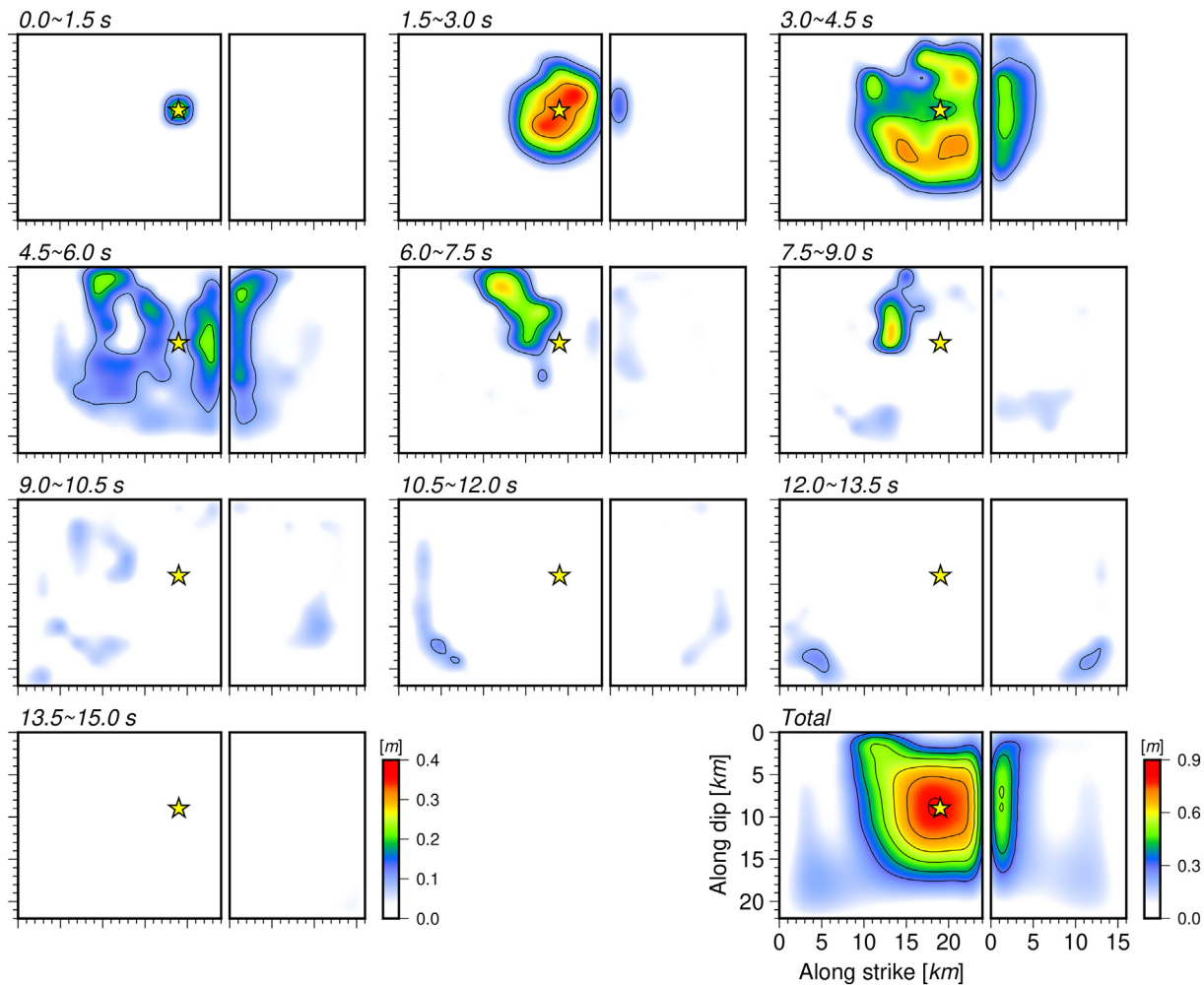


**Fig. 7.** Snapshots of the source rupture process derived from the joint inversion. The lower limit of slip contours plotted in the total slip distribution is 0.3 m, and 0.1 m for other panels. The contour interval is 0.1 m and the yellow star indicates the rupture starting point. (For interpretation of the references to colour in this figure legend, the reader is referred to the web version of this article.)

CFS changes in major active faults via Coulomb 3.3 software (Toda et al., 2011). The effective friction coefficient is intended to include the effects of pore fluids as well as the material properties of the fault zone (Harris, 1998), and a larger value of this coefficient means a larger contribution coming from the normal stress change. When the stress change is dominated by the compression or tension in the fault plane, the friction coefficient can cause a significant CFS change, even its polarity. Most of receiver faults accommodate the accumulated shear or normal stress caused by the eastward motion of the Bayan Har block. The applied stress properties, to some extent, depend on whether the strike of the fault is parallel or perpendicular to the motion of the block. For a more detailed analysis, we calculated the co-seismic CFS changes using several friction coefficients, including 0.1, 0.4 and 0.7.

Fig. 10 shows the co-seismic CFS changes corresponding to different friction coefficients. The geometry and slip sense of receiver faults were adapted from Deng et al. (2003) and Shan et al. (2009). The eastern segment of the Tazang fault lies in a shadow zone. But a positive CFS increase (up to 0.06–0.2 MPa) occurs in the western segment. In a similar situation, the CFS change in the western part of the northern branch of the Tazang fault is positive, while negative in the eastern part. Because the low slip rate led to a sluggish accumulation of interseismic stress (Ren et al., 2013a), the seismicity of the Tazang fault was weak over the past centuries, leaving a gap zone of destructive earthquakes near the easternmost part of the eastern Kunlun fault. Meanwhile, the maximum shear strain rate is stably high in the Maqin-Maqu

segment of the eastern Kunlun fault (Xu et al., 2017). The Jiuzhaigou earthquake has caused further stress loading in the Tazang fault, increasing its seismic hazard in the future. The CFS changes of the Hanan and Wenxian fault to the east of the mainshock are positive, but the increase of CFS is still less than the earthquake triggering threshold of 0.01 MPa (Hardebeck et al., 1998). A linear change of CFS with the change of the friction coefficient is localized in the Bailongjiang fault and the northern segment of the Longriba fault, implying more contribution of the normal stress change. Though CFS in most part of the northern segment of the Minjiang fault is unloading, a small area of increased CFS exceeding 0.2 MPa still exists regardless of the value of the friction coefficient. The historical seismicity of the northern segment of the Minjiang fault was weaker than its southern segment, where the 1933 Dixi  $M_s$  7.5 earthquake happened (Wang et al., 2011). It is difficult to directly evaluate the seismicity trend of the northern segment only depending on the CFS change induced by the Jiuzhaigou earthquake, which is nearly negligible in the southern segment. The polarity of the CFS change in the Xueshanliangzi fault is greatly influenced by the friction coefficient. The CFS of its westernmost part is increased when using a smaller coefficient, but its change even turned into negative when adopting a larger one. The Huya fault, together with the eastern part of the Xueshanliangzi fault, is suffered a positive CFS change. The northern end of the Huya fault is adjacent to the southern segment of the seismogenic fault, and the earthquake has caused obvious stress increase (up to 0.1 MPa) in the northern segment of the

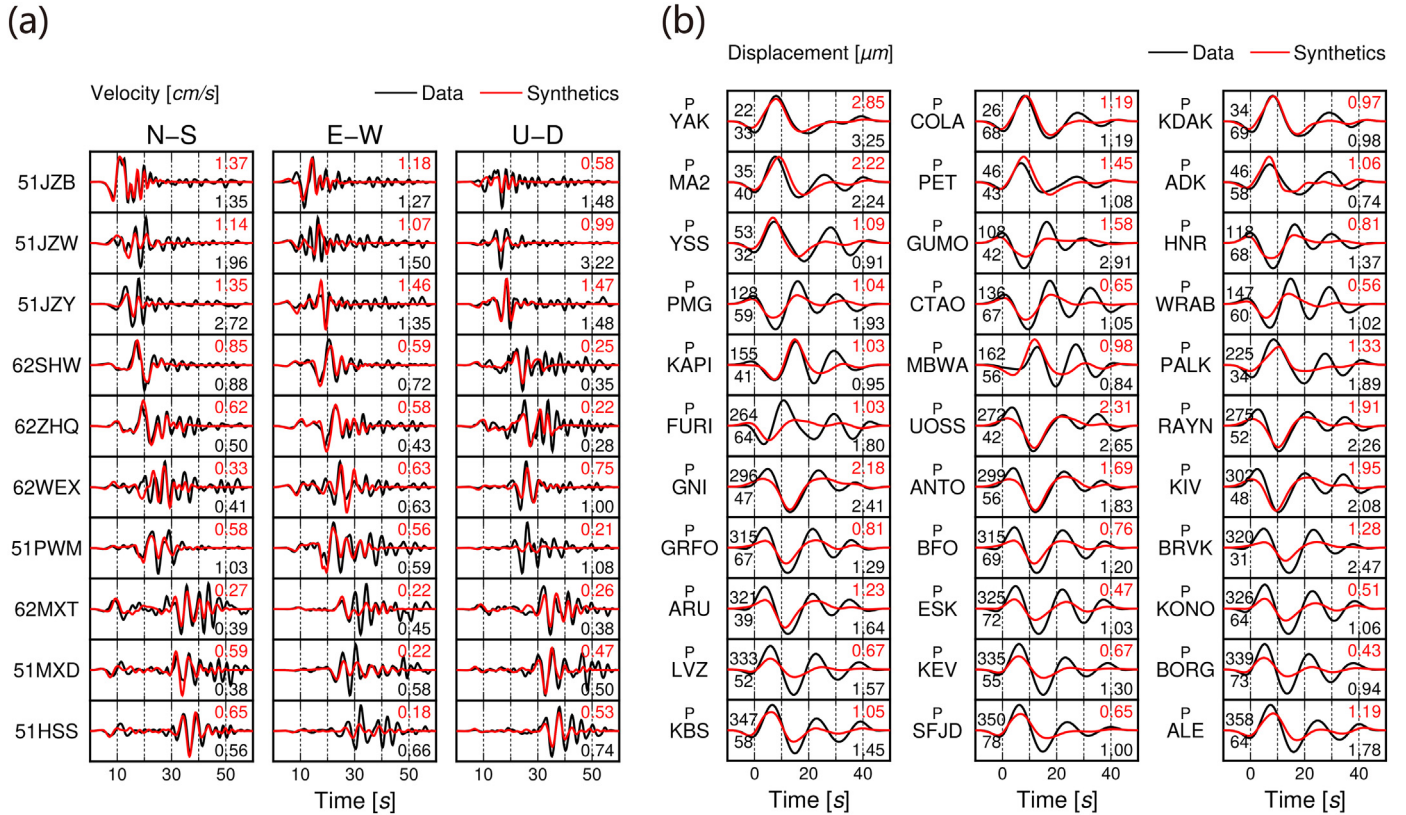


**Fig. 8.** (a) Comparison between the synthetic waveforms obtained from the joint inversion and the observed strong-motion records (velocity). The maximum amplitude of the observed (black font) and synthetic waveform (red font) is shown to the right of each waveform, in centimeters per second. (b) Comparison between the synthetic waveforms and the observed teleseismic  $P$ -wave records (displacement). The maximum amplitude of the observed (black font) and synthetic waveform (red font) is shown to the right of each waveform, in micrometers. The azimuth and distance in degrees are shown at the beginning of each record with the azimuth on top. (For interpretation of the references to colour in this figure legend, the reader is referred to the web version of this article.)

Huya fault. As shown in Fig. 1, the 1973 Songpan-Huanglong  $M_s$  6.5 earthquake and the 1976 Songpan sequence including three earthquakes with  $M_s > 6.5$  implies that the Huya fault may have the potential of accumulating a large amount of tectonic stress (Jones et al., 1984). Moreover, the Jiuzhaigou earthquake has increased the stress loading in the Huya fault, but aftershocks in the corresponding area are quite rare. Thus, the seismic hazard of the Huya fault cannot be ignored. In addition, the CFS change in the Qingchuan fault was also calculated, but it is too small to be thought over.

## 5.2. Seismogenesis associated with regional tectonics

The Jiuzhaigou earthquake occurred in the middle of China's north-south seismic belt, by which the eastern Kunlun fault and the Longmenshan fault belt are connected. As the northern boundary of the Bayan Har block, the eastern Kunlun fault is a major left-lateral strike-slip fault that accommodates and transfers the displacement caused by the eastward motion of the Tibetan Plateau (Xu et al., 2017). Located at the eastern terminus of the eastern Kunlun fault, the Tazang fault is moving at 1.4–3.2 mm/yr based on geological and geodetic data (Ren et al., 2013b). Between the Tazang fault and the Longmenshan fault, the west-dipping Huya fault and Minjiang fault may convert the left-lateral strike slip into the thrust motion. The nearly north-south striking, west dipping Huya fault is thought to be divided into two segments by the east-west striking Xueshanliangzi fault. The dip of the northern segment is  $40^\circ \sim 80^\circ$  and that of the southern segment is  $30^\circ \sim 70^\circ$  (Ren et al., 2017). With a gentler dip, the strike of the southern segment is close to north-south, nearly perpendicular to the motion of the Bayan Har block. It is difficult for the southern segment to continue sustaining strike slip. Thus, the southern segment of the Huya fault is dominated by the thrust

slip, while the northern segment behaves as a left-lateral strike-slip fault. This is consistent with the focal mechanism of the 1973 Songpan-Huanglong earthquake occurred on the northern segment of the Huya fault, while the 1976 Songpan sequence struck the southern segment. The focal mechanism of the Jiuzhaigou earthquake is more similar to that of the 1973 event, whose dense aftershocks distributed along the northern segment of the Huya fault reaching approximately  $33^\circ\text{N}$  (Xu et al., 2017). Hence, the Jiuzhaigou earthquake, the 1973 Songpan-Huanglong earthquake and the 1976 Songpan sequence have formed a north-south trending seismic zone with their aftershocks, filling up the seismic gap left by historical earthquakes. Furthermore, the Minjiang fault and the Huya fault can be considered as the western and eastern boundaries of the Minshan uplift zone, respectively. The newly identified fault that led to the Jiuzhaigou earthquake makes the northeastern boundary of the Minshan uplift zone continuous and more complete.

The eastern Bayan Har block and its vicinity are the leading edges of the Tibetan Plateau, in which the seismicity has been strong during recent years (Deng et al., 2014). At the northeastern margin, the eastern Kunlun fault branches out into a horsetail-shaped structure, and a large part of strike-slip motion is migrated into this structure. The epicenter of the Jiuzhaigou earthquake was located within the northern extension of the Huya fault. Li et al. (2018) used continuous and campaign GPS data acquired after the destructive 2008 Wenchuan earthquake, from 2009 to 2017, to analyze the strain-rate field in the northeastern margin of the Bayan Har block. The results suggested that there was significant strain accumulation in the vicinity of the epicenter before the Jiuzhaigou earthquake, and the shear strain rate was approximately 3.0 mm/yr with an obvious tensile strain rate up to 3.1 mm/yr. Apart from the strike slip, the source mechanism derived from the joint inversion in this study also contains a mixture of normal and thrust slips.

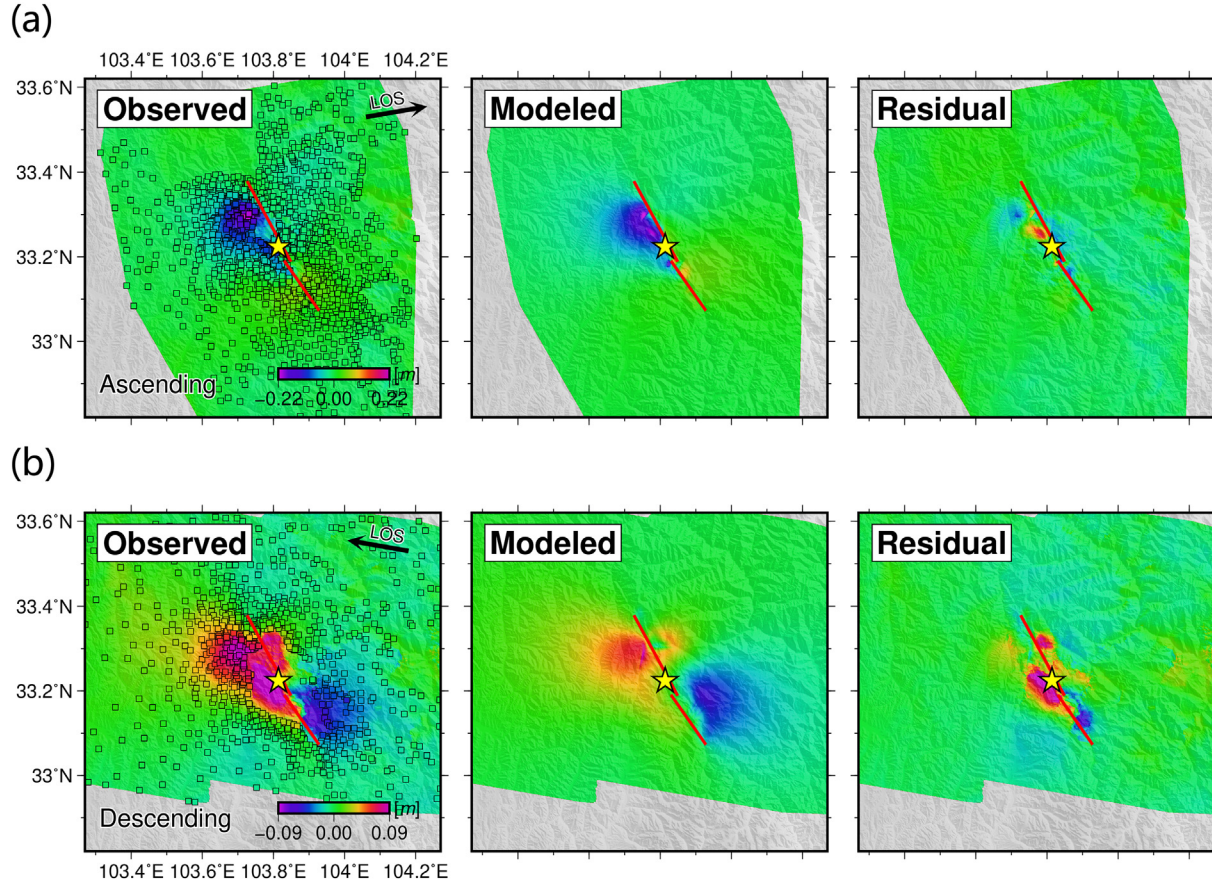


**Fig. 9.** (a) Unwrapped displacement images of the observed, modeled and residual of the co-seismic deformation field acquired by Sentinel-1 in ascending orbit. (b) Unwrapped displacement images of the observed, modeled and residual of the co-seismic deformation field acquired by Sentinel-1 in descending orbit. The black empty squares in observed maps show the subsampled data points. The yellow star indicates the epicenter of the mainshock, and the red lines are the projected top edge traces of the two-segment fault model. (For interpretation of the references to colour in this figure legend, the reader is referred to the web version of this article.)

It is rather strange that normal and thrust slips both occur in a single event. Based on previously proposed evolution models of the Tibetan Plateau, the viscous flow in the middle-to-lower crust was responsible for the uplift of the whole Tibetan Plateau and the extrusion of its eastern margin (Clark et al., 2005; Royden et al., 2008; Sun et al., 2018). Ye et al. (2018) resolved the velocity structure across the Tibet-Qinling transition zone, in which a low velocity body gradually weakened to east, presenting the extruding process of the crustal flow. The eastward expansion of the weak material provided the driving force for lifting the Minshan uplift zone and surrounding regions, accompanying the thrust slip occurred in historical earthquakes of the Huya fault. However, the weak material of the crustal flow is blocked and cut-off by existed faults, also including the seismogenic fault of the Jiuzhaigou event (Ye et al., 2018). Depending on the 3-D inversion of magneto-telluric data, Sun et al. (2019) suggested that the Jiuzhaigou earthquake should be located between the upward-extending high conductivity layer and the high resistivity body near the surface. The depth of the high conductivity layer is greater in the southwest than that in the northeast. Numerous strong earthquakes have occurred within the high resistivity body along the boundary of the high and low resistivity structures (Sun et al., 2019). The mentioned boundary should correspond to the actually existed Huya fault and the seismogenic fault of the Jiuzhaigou earthquake. Considering being situated in such a collision margin of the Bayan Har block, the seismogenic fault should behave as a left-lateral strike-slip fault with thrust motion like the Huya fault. But the invasion of the crustal flow changed the tectonic setting of the region. The invasion and the buoyancy of the crustal flow as well as the eastern motion of the block lifted the area of the hanging-wall side, and

finally generated the Minshan uplift zone. And this process could be accompanied by many tectonic adjustments, such as unrecorded historical earthquakes. The eastward extrusion of the crustal flow is obstructed by the seismogenic fault. But the crustal flow has crossed beyond the fault from the bottom (Ye et al., 2018), therefore, its existence at the eastern side to some extent promoted the lifting of the footwall. Since the crustal flow has just invaded the eastern side of the fault, compared with the hanging-wall side, the squeezing of the invasive material in current stage made the area of the footwall side easier to be lifted or generate more obvious accumulation of tensile strain. This is consistent with the regional strain-rate field revealed by the GPS measurement (Li et al., 2018). The accumulated tensile strain caused and were released in the Jiuzhaigou earthquake, and led to the normal slips that occur in the co-seismic slip distribution. In the deep part of the fault, a few thrust slips came from the motion of the hanging-wall, which was caused in the localized area of squeezing that is closer to the extrusion of the crustal flow and the eastward motion of the block. The co-seismic slip distribution presents the motion of the hanging-wall relative to the footwall. But the normal and thrust slips coexisting in the fault plane, were possibly generated by the absolute motions of the hanging-wall and the footwall respectively. Therefore, such a hybrid mechanism, containing both normal and thrust slips, is not contradictory for a single earthquake event. As illustrated by the conceptual model in Fig. 11, we suggest that the eastward motion with the extrusion of the lower crustal flow in the northeastern margin of the Bayan Har block is responsible for such a hybrid source mechanism of the 2017 Jiuzhaigou earthquake. Considering the continuous extrusion of the crustal flow, we speculate that the area of the footwall side will

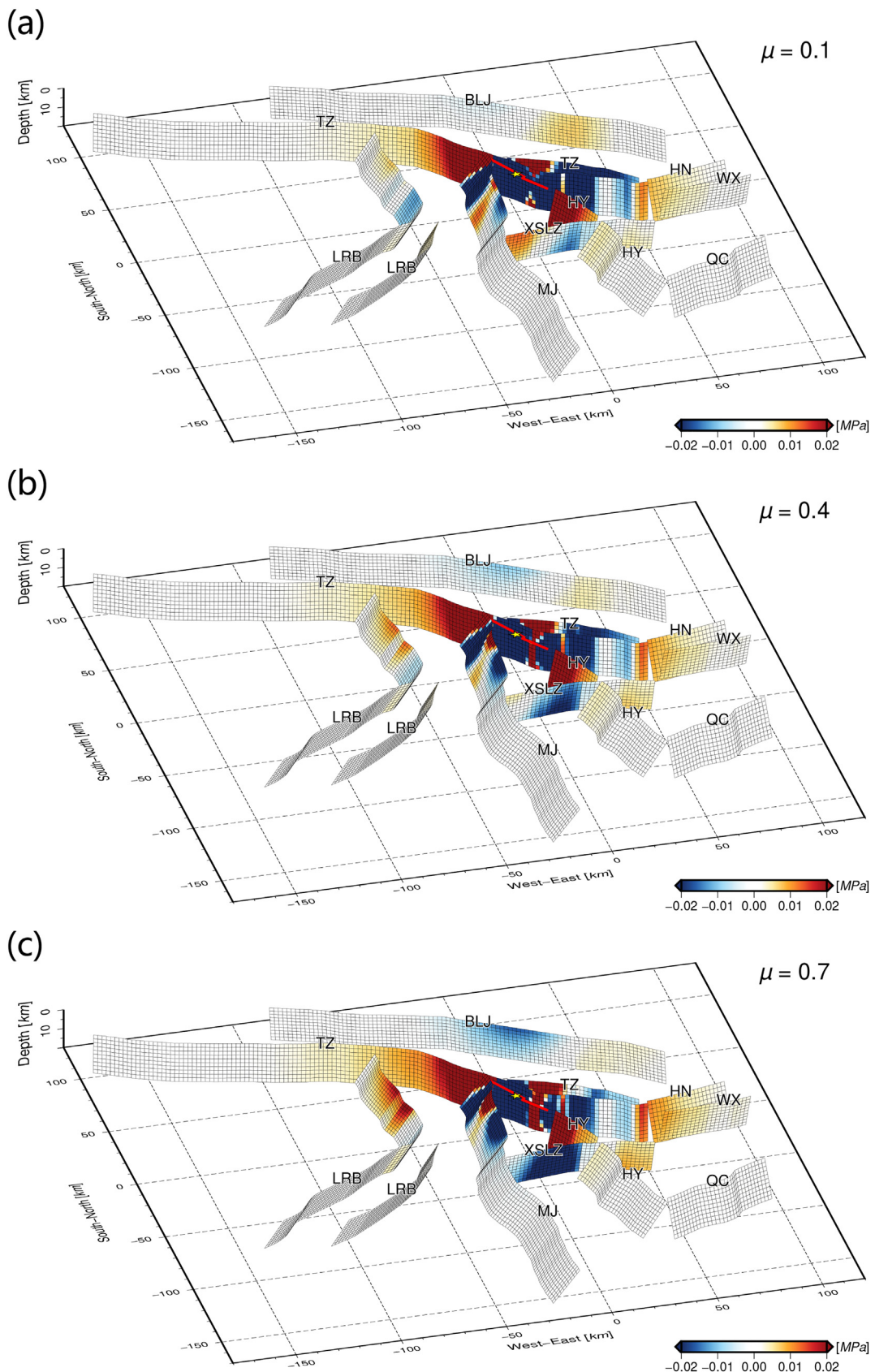


**Fig. 10.** Distributions of the co-seismic CFS changes in surrounding active faults induced by the Jiuzaigou earthquake calculated with three effective friction coefficients. (a) Effective friction coefficient is 0.1. (b) Effective friction coefficient is 0.4. (c) Effective friction coefficient is 0.7. Fault abbreviations are BLJ: Bailongjiang fault, TZ: Tazang fault, LRB: Longriba fault, MJ: Minjiang fault, XSLZ: Xueshanliangzi fault, HY: Huya fault, HN: Hanan fault, WX: Wenxian fault, and QC: Qingchuan fault. (For interpretation of the references to colour in this figure legend, the reader is referred to the web version of this article.)

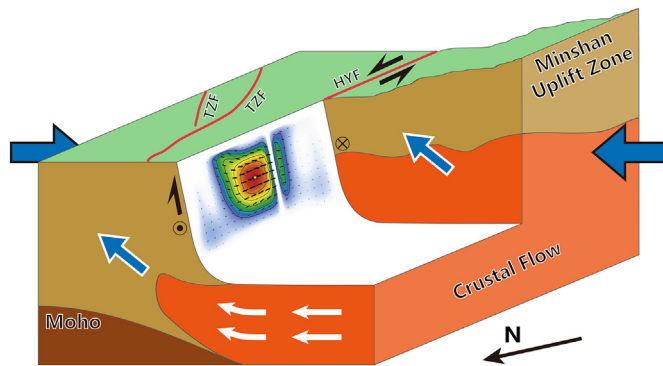


**Fig. 11.** A conceptual model showing the co-seismic slip distribution and seismogenesis of the 2017 Jiuzhaigou earthquake. The crustal flow material has crossed beyond the fault from the bottom, therefore, its existence at the eastern side to some extent promoted the lifting of the footwall. Since the crustal flow has just invaded the eastern side of the fault, compared with the hanging-wall side, the squeezing of the invasive material in current stage made the area of the footwall side easier to be lifted or generate more obvious accumulation of tensile strain. The accumulated tensile strain caused and were released in the Jiuzhaigou earthquake, and led to the normal slips in the co-seismic slip distribution. In the deep part of the fault, a few thrust slips came from the motion of the hanging-wall, which was caused in the localized area of squeezing that is closer to the extrusion of the crustal flow and the eastward motion of the block. Therefore, we suggest that the eastward motion with the extrusion of the lower crustal flow in the northeastern margin of the Bayan Har block is responsible for such a hybrid source mechanism, in which sinistral strike slip, normal and thrust slips all occur during the 2017 Jiuzhaigou earthquake. Fault abbreviations are TZF: Tazang fault, HYF: Huya fault. (For interpretation of the references to colour in this figure legend, the reader is referred to the web version of this article.)

be continuously lifted or cause the accumulation of strain, resulting in an increase of the seismicity in the future. Of course, this inference requires and is also worth of more in-depth investigations, such as the dynamics-based numerical simulation.

## 6. Conclusions

In this study, based on a two-segment fault geometry delineated by the spatial distribution of relocated aftershocks, we investigated the detailed source rupture process of the 2017  $M_w$  6.5 Jiuzhaigou earthquake by the joint inversion of strong-motion, teleseismic body-wave and InSAR data. The maximum co-seismic slip is 0.8 m. The whole rupture process lasts approximately 15 s and releases a seismic moment of  $7.9 \times 10^{18}$  N·m ( $M_w$  6.5). The joint inversion reveals a hybrid source mechanism dominated by left-lateral strike slip with components of both normal and thrust slips. The previously unidentified seismogenic fault is located in the northern extension of the Huya fault and has become an element of the horsetail-shaped structure of the eastern Kunlun fault, making the northeastern boundary of the Minshan uplift zone continuous and more complete. The mainshock and aftershocks of this earthquake have filled up the seismic gap left since the 1973 Songpan-Huanglong earthquake and the 1976 Songpan sequence, forming a north-south trending seismic zone. The material flow in the middle-to-lower crust invaded the northeastern edge of the Bayan Har block, and changed the tectonic setting of this region. The invasion of the crustal flow made the footwall of the seismogenic fault easier to be lifted or generate more obvious accumulation of tensile strain. The accumulated tensile strain was released in the Jiuzhaigou earthquake, and led to the normal slips occurring in the co-seismic slip distribution. In the deep part of the fault, a few thrust slips came from the motion of the hanging-wall, which was caused in the localized area of squeezing that is closer to the extrusion of the crustal flow and the eastward motion of the block. Therefore, we suggest the eastward motion with

the extrusion of the lower crustal flow in the northeastern margin of the Bayan Har block is responsible for such a hybrid source mechanism of the 2017 Jiuzhaigou earthquake. The induced co-seismic CFS changes show a significant stress loading in the western segment of the Tazang fault, increasing its seismic hazard. Due to the lack of aftershocks to the southeast of the seismogenic fault, the probably enhanced seismicity implied by the positive CFS change in the northern segment of the Huya fault is also worth further attention.

## Declaration of competing interest

The authors declare that they have no known competing financial interests or personal relationships that could have appeared to influence the work reported in this paper.

## Acknowledgements

The strong-motion data were recorded by the China Strong Motion Network and accessed through the Institute of Engineering Mechanics, CEA. The teleseismic data were recorded by the International Federation of Digital Seismograph Networks (FDSN), accessed through IRIS DMC. All waveform data were processed by ObsPy (Krischer et al., 2015). This work also used Copernicus data from the Sentinel-1 satellite constellation provided by the European Space Agency (ESA). The InSAR data processing made use of MATLAB and GAMMA software. SRTM DEM data were used for InSAR data processing and map plotting. The observed data sets used in this study, including the preprocessed strong-motion waveforms and subsampled InSAR images, are available as Mendeley Data. Thanks Qian Song, a Ph.D. candidate of the University of Chinese Academy of Sciences, for providing the precisely relocated aftershocks of the Jiuzhaigou earthquake. Thanks Dr. Hannes Vasyura-Bathke for detailed suggestions on using BEAT. The Generic Mapping Tools (GMT) developed by Wessel and Smith (1998) was used to plot the figures. This work was supported by the National Natural Science Foundation of China [grant numbers 41674056, 41804015, 41374105, U1901602, 41790465] and the National Key Research and Development Program of China [grant number 2019YFC1509205]. The comments from two anonymous reviewers and the editor, Dr. Kelin Wang are helpful in improving the manuscript. Here, we would like to express our gratitude together.

## Data availability

Data sets related to this article can be found at <http://dx.doi.org/10.17632/443fbxy23.2>, an open-source online data repository hosted at Mendeley Data (Zheng et al., 2019)

## Appendix A. Supplementary data

Supplementary data to this article can be found online at <https://doi.org/10.1016/j.tecto.2020.228538>.

## References

- Aki, K., Richards, P.G., 2002. Quantitative Seismology, 2nd ed. University Science Books, Sausalito, California.
- Bagnardi, M., Hooper, A., 2018. Inversion of surface deformation data for rapid estimates of source parameters and uncertainties: a Bayesian approach. *Geochem. Geophys. Geosyst.* 19 (7), 2194–2211. <https://doi.org/10.1029/2018gc007585>.
- Beck, J.L., 2010. Bayesian system identification based on probability logic. *Struct. Control. Health Monit.* 17 (7), 825–847. <https://doi.org/10.1002/stc.424>.
- Brocher, T.A., 2005. Empirical relations between elastic wavespeeds and density in the earth's crust. *Bull. Seismol. Soc. Am.* 95 (6), 2081–2092. <https://doi.org/10.1785/0120050077>.
- Chen, C.W., Zebker, H.A., 2001. Two-dimensional phase unwrapping with use of statistical models for cost functions in nonlinear optimization. *J. Opt. Soc. Am. A* 18 (2), 338–351. <https://doi.org/10.1364/josaa.18.000338>.
- Chen, K.J., Xu, W.B., Mai, P.M., Gao, H., Zhang, L., Ding, X.L., 2018. The 2017  $M_w$  7.3 Sarpol Zahab earthquake, Iran: a compact blind shallow-dipping thrust event in the

- mountain front fault basement. *Tectonophysics* 747, 108–114. <https://doi.org/10.1016/j.tecto.2018.09.015>.
- Cheng, J., Rong, Y.F., Magistrale, H., Chen, G.H., Xu, X.W., 2020. Earthquake rupture scaling relations for mainland China. *Seismol. Res. Lett.* 91 (1), 248–261. <https://doi.org/10.1785/0220190129>.
- Ching, J.Y., Chen, Y.C., 2007. Transitional markov chain Monte Carlo method for Bayesian model updating, model class selection, and model averaging. *J. Eng. Mech.* 133 (7), 816–832. [https://doi.org/10.1061/\(ASCE\)0733-9399\(2007\)133:7\(816\)](https://doi.org/10.1061/(ASCE)0733-9399(2007)133:7(816)).
- Clark, M.K., Bush, J.W.M., Royden, L.H., 2005. Dynamic topography produced by lower crustal flow against rheological strength heterogeneities bordering the Tibetan Plateau. *Geophys. J. Int.* 162 (2), 575–590. <https://doi.org/10.1111/j.1365-246X.2005.02580.x>.
- Das, S., Henry, C., 2003. Spatial relation between main earthquake slip and its aftershock distribution. *Rev. Geophys.* 41, 3. <https://doi.org/10.1029/2002rg000119>.
- Delouis, B., Giardini, D., Lundgren, P., Salichon, J., 2002. Joint inversion of InSAR, GPS, teleseismic, and strong-motion data for the spatial and temporal distribution of earthquake slip: application to the 1999 Izmit mainshock. *Bull. Seismol. Soc. Am.* 92 (1), 278–299. <https://doi.org/10.1785/0120000806>.
- Deng, Q.D., Zhang, P.Z., Ran, Y.K., Yang, X.P., Min, W., Chu, Q.Z., 2003. Basic characteristics of active tectonics of China. *Sci. China Ser. D Earth Sci.* 46 (4), 356–372.
- Deng, Q., Cheng, S., Ma, J., Du, P., 2014. Seismic activities and earthquake potential in the Tibetan Plateau. *Chin. J. Geophys. Chin. Ed.* 57 (7), 2025–2042. <https://doi.org/10.6038/cjg20140701>.
- Dutta, R., Jonsson, S., Wang, T., Vasyura-Bathke, H., 2018. Bayesian estimation of source parameters and associated Coulomb failure stress changes for the 2005 Fukuoka (Japan) Earthquake. *Geophys. J. Int.* 213 (1), 261–277. <https://doi.org/10.1093/gji/ggx551>.
- Farr, T.G., Rosen, P.A., Caro, E., Crippen, R., Duren, R., Hensley, S., et al., 2007. The shuttle radar topography mission. *Rev. Geophys.* 45 (2). <https://doi.org/10.1029/2005rg000183>.
- Funning, G.J., Fukahata, Y., Yagi, Y., Parsons, B., 2014. A method for the joint inversion of geodetic and seismic waveform data using ABIC: application to the 1997 Manyi, Tibet, earthquake. *Geophys. J. Int.* 196 (3), 1564–1579. <https://doi.org/10.1093/gji/ggt406>.
- Hardebeck, J.L., Nazareth, J.J., Hauksson, E., 1998. The static stress change triggering model: constraints from two southern California aftershock sequences. *J. Geophys. Res. Solid Earth* 103 (B10), 24427–24437. <https://doi.org/10.1029/98jb00573>.
- Harris, R.A., 1998. Introduction to special section: stress triggers, stress shadows, and implications for seismic hazard. *J. Geophys. Res. Solid Earth* 103 (B10), 24347–24358. <https://doi.org/10.1029/98jb01576>.
- Hartzell, S.H., Heaton, T.H., 1983. Inversion of strong ground motion and teleseismic waveform data for the fault rupture history of the 1979 Imperial Valley, California, earthquake. *Bull. Seismol. Soc. Am.* 73 (6), 1553–1583.
- Heimann, S., Kriegerowski, M., Isken, M., Cesca, S., Daout, S., Grigoli, F., et al., 2017. Pyrocko—an Open-Source Seismology Toolbox and Library. GFZ Data Services <https://doi.org/10.5880/GFZ.2.1.2017.001>.
- Jaynes, E.T., 2003. Probability Theory: The Logic of Science. Cambridge University Press, Cambridge.
- Jeffreys, H., 1983. Theory of Probability, 3rd ed. Clarendon Press, Oxford.
- Ji, L., Liu, C., Xu, J., Liu, L., Long, F., Zhang, Z., 2017. InSAR observation and inversion of the seismogenic fault for the 2017 Jiuzhaigou Ms 7.0 earthquake in China. *Chin. J. Geophys. Chin. Ed.* 60 (10), 4069–4082. <https://doi.org/10.6038/cjg20171032>.
- Jones, L.M., Han, W.B., Hauksson, E., Jin, A.S., Zhang, Y.G., Luo, Z.L., 1984. Focal mechanisms and aftershock locations of the Songpan earthquakes of August 1976 in Sichuan, China. *J. Geophys. Res.* 89 (NB9), 7697–7707. <https://doi.org/10.1029/JB089iB09p07697>.
- Jónsson, S., Zebker, H., Segall, P., Amelung, F., 2002. Fault slip distribution of the 1999 Mw 7.1 Hector Mine, California, earthquake, estimated from satellite radar and GPS measurements. *Bull. Seismol. Soc. Am.* 92 (4), 1377–1389. <https://doi.org/10.1785/0120000922>.
- Kanamori, H., Anderson, D.L., 1975. Theoretical basis of some empirical relations in seismology. *Bull. Seismol. Soc. Am.* 65 (5), 1073–1095.
- Kennett, B.L.N., Engdahl, E.R., Buland, R., 1995. Constraints on seismic velocities in the earth from travel-times. *Geophys. J. Int.* 122 (1), 108–124. <https://doi.org/10.1111/j.1365-246X.1995.tb03540.x>.
- King, G.C.P., Stein, R.S., Lin, J., 1994. Static stress changes and the triggering of earthquakes. *Bull. Seismol. Soc. Am.* 84 (3), 935–953.
- Krischer, L., Megies, T., Barsch, R., Beyreuther, M., Lecocq, T., Caudron, C., et al., 2015. ObsPy: a bridge for seismology into the scientific Python ecosystem. *Comput. Sci. Disc.* 8 (1), 014003. <https://doi.org/10.1088/1749-4699/8/1/014003>.
- Laske, G., Masters, G., Ma, Z., Pasyanos, M., 2013. Update on CRUST1. 0 – A 1-degree global model of Earth's crust. In: Paper Presented at the 2013 EGU General Assembly, Vienna, Austria.
- Lawson, C.L., Hanson, R.J., 1974. Solving Least Squares Problems. Prentice-Hall, Englewood Cliffs, London.
- Li, Z.W., Ding, X., Huang, C., Zhu, J.J., Chen, Y.L., 2008. Improved filtering parameter determination for the Goldstein radar interferogram filter. *ISPRS J. Photogramm. Remote Sens.* 63 (6), 621–634. <https://doi.org/10.1016/j.isprsjprs.2008.03.001>.
- Li, C., Su, X., Meng, G., 2018. Heterogeneous strain rate field in the northeast margin of Bayan Har Block from GPS observations and its relationship with the 2017 Jiuzhaigou Ms 7.0 earthquake. *Earthquake* 38 (2), 37–50. <https://doi.org/10.3969/j.issn.1000-3274.2018.02.004>.
- Liu, X.G., Xu, W.B., 2019. Logarithmic model joint inversion method for coseismic and postseismic slip: application to the 2017 Mw 7.3 Sarpol Zahab Earthquake, Iran. *J. Geophys. Res. Solid Earth* 124 (11), 12034–12052. <https://doi.org/10.1029/2019jb017953>.
- Liu, M., Mooney, W.D., Li, S., Okaya, N., Detweiler, S., 2006. Crustal structure of the northeastern margin of the Tibetan plateau from the Songpan-Ganzi terrane to the Ordos basin. *Tectonophysics* 420 (1–2), 253–266. <https://doi.org/10.1016/j.tecto.2006.01.025>.
- Massonnet, D., Rossi, M., Carmona, C., Adragna, F., Peltzer, G., Feigl, K., et al., 1993. The displacement field of the Landers earthquake mapped by radar interferometry. *Nature* 364 (6433), 138–142. <https://doi.org/10.1038/364138a0>.
- Melgar, D., Bock, Y., 2015. Kinematic earthquake source inversion and tsunami runup prediction with regional geophysical data. *J. Geophys. Res. Solid Earth* 120 (5), 3324–3349. <https://doi.org/10.1002/2014jb011832>.
- Metropolis, N., Rosenbluth, A.W., Rosenbluth, M.N., Teller, A.H., Teller, E., 1953. Equation of state calculations by fast computing machines. *J. Chem. Phys.* 21 (6), 1087–1092. <https://doi.org/10.1063/1.1699114>.
- Minson, S.E., Simons, M., Beck, J.L., 2013. Bayesian inversion for finite fault earthquake source models I-theory and algorithm. *Geophys. J. Int.* 194 (3), 1701–1726. <https://doi.org/10.1093/gji/ggt180>.
- Nie, Z., Wang, D.J., Jia, Z., Yu, P., Li, L., 2018. Fault model of the 2017 Jiuzhaigou Mw 6.5 earthquake estimated from coseismic deformation observed using Global Positioning System and Interferometric Synthetic Aperture Radar data. *Earth Planet. Space* 70. <https://doi.org/10.1186/s40623-018-0826-4>.
- Olson, A.H., Apsel, R.J., 1982. Finite faults and inverse-theory with applications to the 1979 Imperial Valley earthquake. *Bull. Seismol. Soc. Am.* 72 (6), 1969–2001.
- Qian, Y.Y., Ni, S.D., Wei, S.J., Almeida, R., Zhang, H., 2017. The effects of core-reflected waves on finite fault inversions with teleseismic body wave data. *Geophys. J. Int.* 211 (2), 936–951. <https://doi.org/10.1093/gji/ggx338>.
- Ren, J., Xu, X., Yeats, R.S., Zhang, S., 2013a. Latest Quaternary paleoseismology and slip rates of the Longriba fault zone, eastern Tibet: implications for fault behavior and strain partitioning. *Tectonics* 32 (2), 216–238. <https://doi.org/10.1002/tect.20029>.
- Ren, J., Xu, X., Yeats, R.S., Zhang, S., 2013b. Millennial slip rates of the Tazang fault, the eastern termination of Kunlun fault: implications for strain partitioning in eastern Tibet. *Tectonophysics* 608, 1180–1200. <https://doi.org/10.1016/j.tecto.2013.06.026>.
- Ren, J., Xu, X., Zhang, S., Luo, Y., Liang, O., Zhao, J., 2017. Tectonic transformation at the eastern termination of the Eastern Kunlun fault zone and seismogenic mechanism of the 8 August 2017 Jiuzhaigou Ms 7.0 earthquake. *Chin. J. Geophys. Chin. Ed.* 60 (10), 4027–4045. <https://doi.org/10.6038/cjg20171029>.
- Royden, L.H., Burchfiel, B.C., Van Der Hilst, R.D., 2008. The geological evolution of the Tibetan plateau. *Science* 321 (5892), 1054–1058. <https://doi.org/10.1126/science.1155371>.
- Sekiguchi, H., Iwata, T., 2002. Rupture process of the 1999 Kocaeli, Turkey, earthquake estimated from strong-motion waveforms. *Bull. Seismol. Soc. Am.* 92 (1), 300–311. <https://doi.org/10.1785/0120000811>.
- Sekiguchi, H., Irikura, K., Iwata, T., 2000. Fault geometry at the rupture termination of the 1995 Hyogo-ken Nanbu earthquake. *Bull. Seismol. Soc. Am.* 90 (1), 117–133. <https://doi.org/10.1785/0119990027>.
- Shan, B., Xiong, X., Zheng, Y., Diao, F.Q., 2009. Stress changes on major faults caused by Mw 7.9 Wenchuan earthquake, May 12, 2008. *Sci. China Ser. D Earth Sci.* 52 (5), 593–601. <https://doi.org/10.1007/s11430-009-0060-9>.
- Shan, X., Qu, C., Gong, W., Zhao, D., Zhang, Y., Zhang, G., et al., 2017. Coseismic deformation field of the Jiuzhaigou Ms 7.0 earthquake from Sentinel-1A InSAR data and fault slip inversion. *Chin. J. Geophys. Chin. Ed.* 60 (12), 4527–4536. <https://doi.org/10.6038/cjg20171201>.
- Shen, W., Ritzwoller, M.H., Kang, D., Kim, Y.H., Lin, F.C., Ning, J., et al., 2016. A seismic reference model for the crust and uppermost mantle beneath China from surface wave dispersion. *Geophys. J. Int.* 206 (2), 954–979. <https://doi.org/10.1093/gji/ggw175>.
- Song, Q., Yu, X., Zhang, W., Deng, S., 2019. An accurate relocation of the 2017 Ms 7.0 Sichuan Jiuzhaigou earthquake sequence and the seismicity analysis. In: Paper Presented at the 2019 AGU Fall Meeting, San Francisco, CA.
- Stein, R.S., King, G.C.P., Lin, J., 1994. Stress triggering of the 1994 M = 6.7 Northridge, California, earthquake by its predecessors. *Science* 265 (5177), 1432–1435. <https://doi.org/10.1126/science.265.5177.1432>.
- Sun, J.B., Yue, H., Shen, Z.K., Fang, L.H., Zhan, Y., Sun, X.Y., 2018. The 2017 Jiuzhaigou earthquake: complicated event occurred in a young fault system. *Geophys. Res. Lett.* 45 (5), 2230–2240. <https://doi.org/10.1002/2017gl076421>.
- Sun, X.Y., Zhan, Y., Zhao, L.Q., Chen, X.B., Sun, J.B., Li, C.X., et al., 2019. Electrical structure of the Kunlun-Qinling fault system, northeastern Tibetan Plateau, inferred from 3-D inversion of magnetotelluric data. *J. Asian Earth Sci.* 181. <https://doi.org/10.1016/j.jseaes.2019.103910>.
- Tarantola, A., 2005. Inverse Problem Theory and Methods for Model Parameter Estimation. Society for Industrial and Applied Mathematics, Philadelphia, Pennsylvania.
- Toda, S., Stein, R.S., Sevilgen, V., Lin, J., 2011. Coulomb 3.3 graphic-rich deformation and stress-change software for earthquake, tectonic, and volcano research and teaching-user guide. In: U.S. Geological Survey Open-File Report 2011-1060.
- Ulrych, T.J., Sacchi, M.D., Woodbury, A., 2001. A Bayes tour of inversion: a tutorial. *Geophysics* 66 (1), 55–69. <https://doi.org/10.1190/1.1444923>.
- Vasyura-Bathke, H., Dettmer, J., Steinberg, A., Heimann, S., Isken, M.P., Zielke, O., et al., 2020. The Bayesian earthquake analysis tool. *Seismol. Res. Lett.* 91 (2A), 1003–1018. <https://doi.org/10.1785/0220190075>.
- Wald, D.J., Heaton, T.H., Hudnut, K.W., 1996. The slip history of the 1994 Northridge, California, earthquake determined from strong-motion, teleseismic, GPS, and leveling data. *Bull. Seismol. Soc. Am.* 86 (1), S49–S70.
- Wang, C.Y., Han, W.B., Wu, J.P., Lou, H., Chan, W.W., 2007. Crustal structure beneath the eastern margin of the Tibetan Plateau and its tectonic implications. *J. Geophys. Res. Solid Earth* 112 (B7). <https://doi.org/10.1029/2005jb003873>.

- Wang, Q., Qiao, X., Lan, Q., Freymueller, J., Yang, S., Xu, C., et al., 2011. Rupture of deep faults in the 2008 Wenchuan earthquake and uplift of the Longmen Shan. *Nat. Geosci.* 4 (9), 634–640. <https://doi.org/10.1038/ngeo1210>.
- Weng, H.H., Yang, H.F., 2017. Seismogenic width controls aspect ratios of earthquake ruptures. *Geophys. Res. Lett.* 44 (6), 2725–2732. <https://doi.org/10.1002/2016gl072168>.
- Wessel, P., Smith, W.H.F., 1998. New, improved version of Generic Mapping Tools released. *EOS Trans. Am. Geophys. Union* 79 (47), 579.
- Xie, Z., Zheng, Y., Yao, H., Fang, L., Zhang, Y., Liu, C., et al., 2018. Preliminary analysis on the source properties and seismogenic structure of the 2017 Ms 7.0 Jiuzhaigou earthquake. *Sci. China Earth Sci.* 61 (3), 339–352. <https://doi.org/10.1007/s11430-017-9161-y>.
- Xu, W., 2017. Finite-fault slip model of the 2016 Mw 7.5 Chiloé earthquake, southern Chile, estimated from Sentinel-1 data. *Geophys. Res. Lett.* 44 (10), 4774–4780. <https://doi.org/10.1002/2017gl073560>.
- Xu, W., Jónsson, S., Ruch, J., Aoki, Y., 2016. The 2015 Wolf volcano (Galapagos) eruption studied using Sentinel-1 and ALOS-2 data. *Geophys. Res. Lett.* 43 (18), 9573–9580. <https://doi.org/10.1002/2016gl069820>.
- Xu, X., Chen, G., Wang, Q., Chen, L., Ren, Z., Xu, C., et al., 2017. Discussion on seismogenic structure of Jiuzhaigou earthquake and its implication for current strain state in the southeastern Qinghai-Tibet Plateau. *Chin. J. Geophys. Chin. Ed.* 60 (10), 4018–4026. <https://doi.org/10.6038/cjg20171028>.
- Xu, W., Feng, G., Meng, L., Zhang, A., Ampuero, J.P., Bürgmann, R., et al., 2018. Transpressional rupture cascade of the 2016 Mw 7.8 Kaikoura earthquake, New Zealand. *J. Geophys. Res. Solid Earth* 123 (3), 2396–2409. <https://doi.org/10.1002/2017jb015168>.
- Yagi, Y., Mikumo, T., Pacheco, J., Reyes, G., 2004. Source rupture process of the Tecoman, Colima, Mexico earthquake of 22 January 2003, determined by joint inversion of teleseismic body-wave and near-source data. *Bull. Seismol. Soc. Am.* 94 (5), 1795–1807. <https://doi.org/10.1785/012003095>.
- Ye, Z., Gao, R., Li, Q., Xu, X., Huang, X., Xiong, X., et al., 2018. Eastward extrusion and northward expansion of the Tibetan Plateau-Discussions for the deep processes of the plateau uplift. *Chin. Sci. Bull.* 63 (0023–074X), 3217–3228. <https://doi.org/10.1360/N972018-00478>.
- Yi, G., Long, F., Liang, M., Zhang, H., Zhao, M., Ye, Y., et al., 2017. Focal mechanism solutions and seismogenic structure of the 8 August 2017 M7.0 Jiuzhaigou earthquake and its aftershocks, northern Sichuan. *Chin. J. Geophys. Chin. Ed.* 60 (10), 4083–4097. <https://doi.org/10.6038/cjg20171033>.
- Zhang, X., Feng, W., Xu, L., Li, C., 2017. The source-process inversion and the intensity estimation of the 2017 Ms 7.0 Jiuzhaigou earthquake. *Chin. J. Geophys. Chin. Ed.* 60 (10), 4105–4116. <https://doi.org/10.6038/cjg20171035>.
- Zhao, D., Qu, C., Shan, X., Gong, W., Zhang, Y., Zhang, G., 2018. InSAR and GPS derived coseismic deformation and fault model of the 2017 Ms 7.0 Jiuzhaigou earthquake in the Northeast Bayanhar block. *Tectonophysics* 726, 86–99. <https://doi.org/10.1016/j.tecto.2018.01.026>.
- Zheng, A., Wang, M., Yu, X., Zhang, W., 2018. Source rupture process of the 2016 Kaikoura, New Zealand earthquake estimated from the kinematic waveform inversion of strong-motion data. *Geophys. J. Int.* 212 (3), 1736–1746. <https://doi.org/10.1093/gji/ggx505>.
- Zheng, A., Yu, X., Xu, W., Chen, X., Zhang, W., 2019. A hybrid source mechanism of the 2017 Mw 6.5 Jiuzhaigou earthquake revealed by the joint inversion of strong-motion, teleseismic and InSAR data. *Datasets*. <https://doi.org/10.17632/443fbxy23.2>.
- Zhu, L., Rivera, L.A., 2002. A note on the dynamic and static displacements from a point source in multilayered media. *Geophys. J. Int.* 148 (3), 619–627. <https://doi.org/10.1046/j.1365-246X.2002.01610.x>.